Inorganic Chemistry

pubs.acs.org/IC Article

Increasing Anticancer Activity with Phosphine Ligation in Zwitterionic Half-Sandwich Iridium(III), Rhodium(III), and Ruthenium(II) Complexes

Xueyan Hu, Lihua Guo,* Mengqi Liu, Qiuya Zhang, Yuwen Gong, Mengru Sun, Shenghan Feng, Youzhi Xu, Yiming Liu, and Zhe Liu*

Cite This: *Inorg. Chem.* 2022, 61, 20008−20025 Read Online

ACCESS | Metrics & More | Article Recommendations | Supporting Information

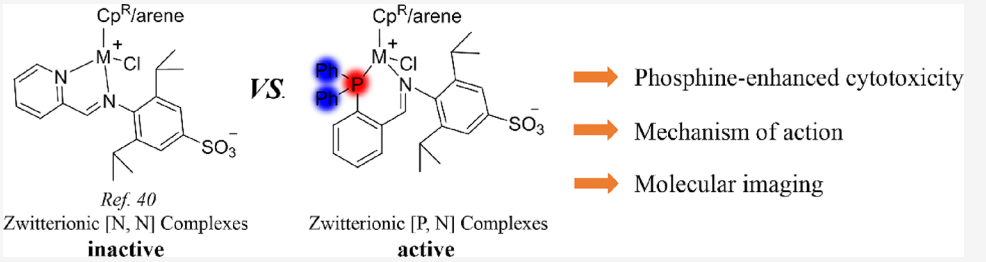

ABSTRACT: The synthesis and biological assessment of neutral or cationic platinum group metal-based anticancer complexes have been extremely studied, whereas there are few reports on the corresponding zwitterionic complexes. Herein, the synthesis, characterization, and bioactivity of zwitterionic half-sandwich phosphine−imine iridium(III), rhodium(III), and ruthenium(II) complexes were presented. The sulfonated phosphine−imine ligand and a group of zwitterionic half-sandwich *P,N*-chelating organometallic complexes were fully characterized by nuclear magnetic resonance (NMR), mass spectrum (electrospray ionization, ESI), elemental analysis, and X-ray crystallography. The solution stability of these complexes and their spectral properties were also determined. Notably, almost all of these complexes showed enhanced anticancer activity against model HeLa and A549 cancer cells than the corresponding zwitterionic pyridyl−imine *N,N*-chelating iridium(III) and ruthenium(II) complexes, which have exhibited inactive or low active in our previous work. The increase in the lipophilic property and intracellular uptake levels of these zwitterionic *P,N*-chelating complexes appeared to be associated with their superior cytotoxicity. In addition, these complexes showed biomolecular interactions with bovine serum albumin (BSA). The flow cytometry studies indicated that the representative complex **Ir1** could induce early-stage apoptosis in A549 cells. Further, confocal microscopy imaging analysis displayed that **Ir1** entered A549 cells through the energy-dependent pathway, targeted lysosome, and could cause lysosomal damage. In particular, these complexes could impede cell migration in A549 cells.

1. INTRODUCTION

Cancer has been a common disease with high incidence, which is widely perceived as one of the leading reasons of death.[1,2] Although a series of platinum antitumor drugs such as cisplatin and its derivatives have been applied in clinical practice, the serious side effects have made scientists commit themselves to searching for more efficient and less toxic antitumor drugs.[3−8] The tumor-killing agents of a number of platinum family metals with reduced side effects and excellent anticancer activity have been widely concerned.[9−20] The ruthenium complexes NAMI-A and KP1019 have shown the most promising results in preclinical and clinical trials.[21,22] Recently, the organometallic platinum group metal compounds offer rich versatility for the rational design of anticancer complexes. According to the structure type, these platinum group metal-based anticancer complexes can be divided into two main groups: cyclometalated complexes and half-sandwich complexes (Scheme 1). Over the past few years, cyclometalated complexes have been gaining popular attention due to their excellent luminescence nature and pretty good cytotoxic efficacy under light, which afforded quite a wide range of applications for photodynamic therapy (PDT), molecular imaging, and bioprobes.[23,24] Recently, half-sandwich iridium(III), rhodium(III), ruthenium(II), and osmium(II) organometallic anticancer complexes with the structure type $[(\eta^6\text{-arene})/(\eta^5\text{-Cp*})M(XY)Cl]^{0/+}$ (Cp*: $C_5(CH_3)_5$; M: Ir, Rh, Ru, Os; XY: bidentate chelating ligands) have attracted

Received: September 15, 2022
Published: November 25, 2022

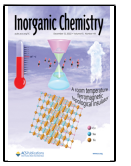

https://doi.org/10.1021/acs.inorgchem.2c03279
Inorg. Chem. 2022, 61, 20008−20025

Scheme 1. Cyclometalated Complexes and Half-Sandwich Complexes

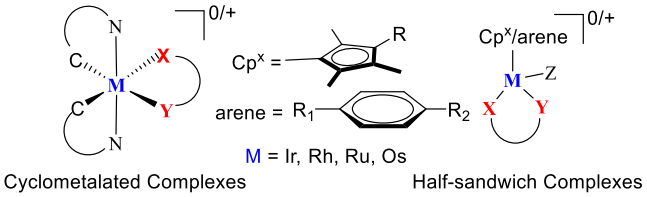

widespread attention due to their amenable coordination structure and different mechanisms of action (MoAs) with platinum drugs.[25−28] Most of these studies concentrated on the preparation and application of neutral and cationic anticancer complexes with various bidentate XY ligands.[29−34] For example, the Sadler group has shown that switching on the cytotoxic potency of the corresponding iridium(III) complexes could be realized by replacing neutral *N*,*N*-chelating ligand (2,2′-bipyridine) with the negatively charged anionic *C*,*N*-chelating ligand (2-phenylpyridine) (Scheme 2, **I** and **II**).[33,35−38] Our group have also systematically investigated the counteranion effect on the cytotoxicity and biological activity of the cationic half-sandwich iridium(III) complexes (Scheme 2, **III**).[39] The above-mentioned studies indicated that the charge of the metal center, the substitution model of the chelate ligands, and the counteranion have a great influence on chemical reactivity and anticancer activity of the complexes. Hence, our group subsequently have prepared a group of rarely reported zwitterionic iridium(III) and ruthenium(II) complexes and investigated their biological activity (Scheme 2, **IV**).[40] Unfortunately, these zwitterionic half-sandwich complexes were inactive, which may be mainly due to their low hydrophobicity.[40] The introduction of fluorinated substituents into zwitterionic complexes seemed to be a feasible strategy to improve the hydrophobicity, thus leading to increased anticancer activity.[41] However, these pyridyl−imine zwitterionic complexes still showed no or low anticancer activity compared to the commercial cisplatin. Therefore, this prompted us to increase their anticancer activity through further structural modification.

In the last few years, organometallic anticancer complexes bearing phosphine-containing chelating ligand have become a new approach to adjust the chemical and biological properties.[42−45] A typical example is RAPTA family (e.g., RAPTA-C; Scheme 2, **V**) containing 1,3,5-triaza-7-phosphatricyclo[3.3.1.1.]decane ligand and Ru−arene complexes,[46,47] which has been at an advanced preclinical trial.[48] Previous studies have showed that the presence of phosphine ligands could increase membrane permeability and the lipophilicity of the anticancer complexes to gain cytotoxicity.[49−51] Consequently, we have become interested in whether the introduction of phosphine into zwitterionic complexes could increase cytotoxicity. Additionally, the introduction of lipophilic phenyl rings in phosphine ligands may also give rise to the enhanced anticancer activity of the corresponding complexes. In particular, the zwitterionic coordination mode with lipophilic phosphine ligation may increase the cellular accumulation and even the possibility to target organelles. Based on these considerations, we herein describe the preparation, characterization, and biological assessment of a group of zwitterionic phosphine−imine half-sandwich iridium(III), rhodium(III), and ruthenium(II) organometallic complexes (Scheme 2). Furthermore, the phosphine-enhanced cytotoxicity of zwitterionic complexes, mechanisms of action, and molecular imaging have also been discussed.

2. RESULTS AND DISCUSSION

2.1. Syntheses and Characterizations. Sulfonated phosphine−imine ligand **L** was synthesized in a 58% isolated yield by a Schiff base reaction of sodium 2,6-diisopropylaniline sulfonate with 2-(diphenylphosphinyl) benzaldehyde (Scheme 3). This ligand can be readily purified by recrystallization from methanol and subsequent diethyl ether washing. In the ^{1}H NMR spectra, the characteristic peak of **L** was at 8.72 ppm (Figure S3), which was assigned to the hydrogen of double bonds of the C*H*═N group. The structure of **L** was also confirmed by ^{31}P{^{1}H} NMR (Figure S4), ^{13}C{^{1}H} NMR (Figure S5), and mass spectrometry (Figure S36).

The bimetallic iridium(III), rhodium(III), and ruthenium(II) precursors $[(\eta^5\text{-}C_5Me_5)MCl_2]_2$ (M = Ir (**D1**); Rh (**D5**)),

Scheme 2. Reported Organometallic Half-Sandwich Complexes and Our Current Work

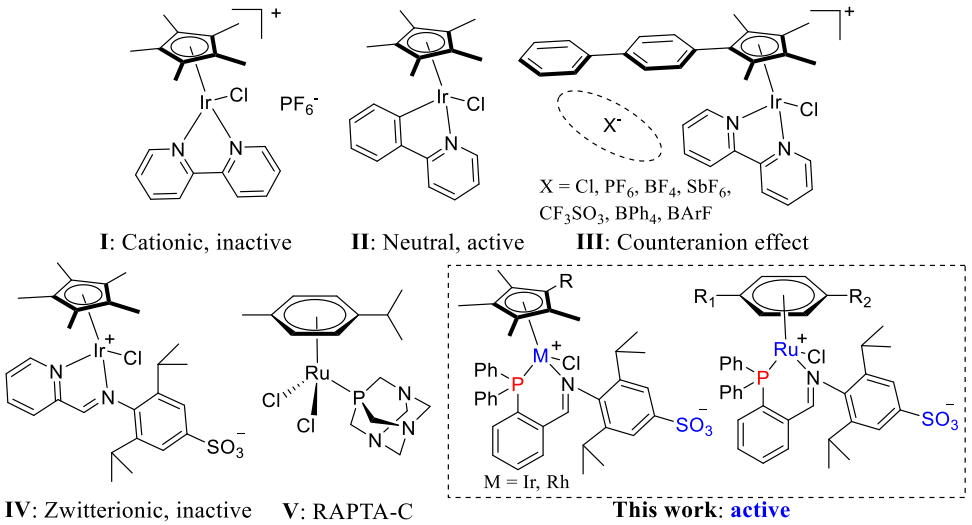

https://doi.org/10.1021/acs.inorgchem.2c03279
Inorg. Chem. 2022, 61, 20008−20025

Scheme 3. Syntheses of Ligand L and Complexes Ir1−Ir4, Rh1−Rh3, and Ru1−Ru3

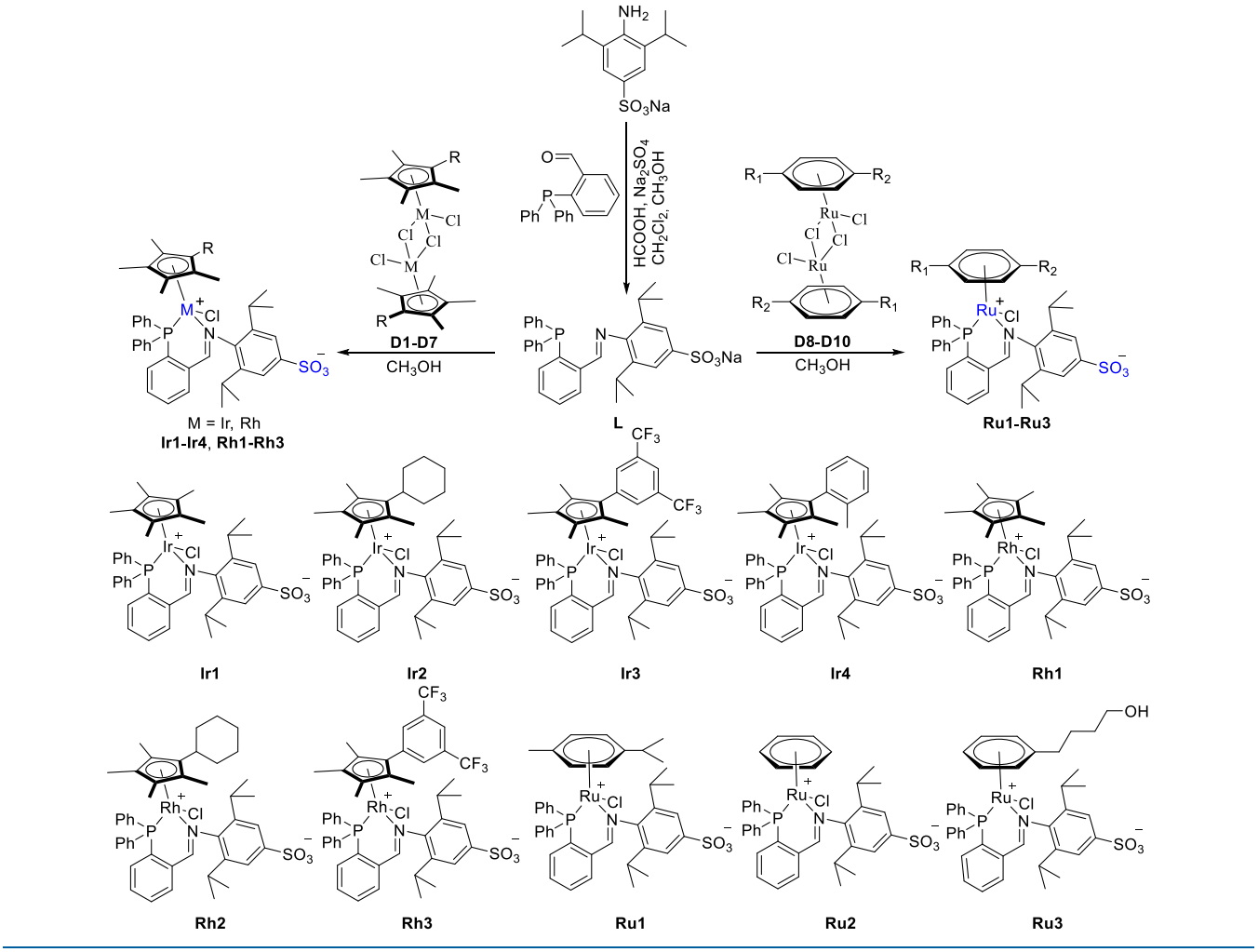

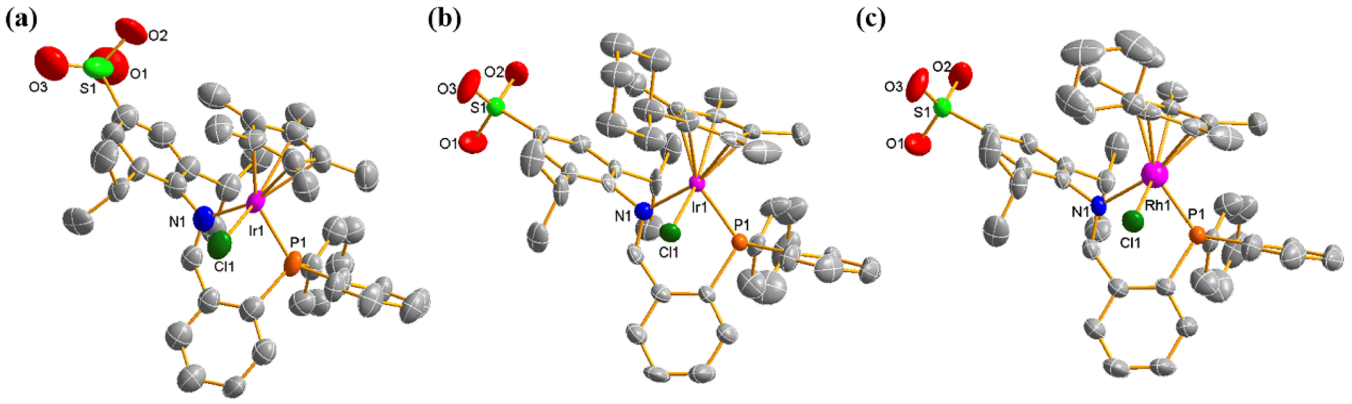

Figure 1. X-ray crystal structures of complexes (a) **Ir1**, (b) **Ir2**, and (c) **Rh2** with the thermal ellipsoids drawn at the 50% probability level. The hydrogen atoms have been omitted for clarity. (a) Bond angles around Ir(III) ion (deg): N1−Ir1−P1 = 88.2(5), P1−Ir1−Cl1 = 90.2(2), N1−Ir1−Cl1 = 88.0(5). Bond lengths (Å): Ir1−C(centroid) = 2.0144, Ir1−P1 = 2.260(6), Ir1−N1 = 2.06(2), Ir1−Cl1 = 2.360(6). (b) Bond angles around Ir(III) ion (deg): N1−Ir1−P1 = 85.2(2), P1−Ir1−Cl1 = 88.17(9), N1−Ir1−Cl1 = 85.3(2). Bond lengths (Å): Ir1−C(centroid) = 1.8448, Ir1−P1 = 2.280(3), Ir1−N1 = 2.132(8), Ir1−Cl1 = 2.409(2). (c) Bond angles around Rh(III) ion (deg): N1−Rh1−P1 = 84.56(6), P1−Rh1−Cl1 = 88.64(3), N1−Rh1−Cl1 = 87.30(6). Bond lengths (Å): Rh1−C(centroid) = 1.8587, Rh1−P1 = 2.3128(7), Rh1−N1 = 2.181(2), Rh1−Cl1 = 2.4292(7).

$[(\eta^5\text{-Cp}^R)MCl_2]_2$ ($Cp^R = C_5(CH_3)_4R$, R = Cy (M = Ir (**D2**); M = Rh (**D6**)), 2-methylbenzene (M = Ir (**D4**)), 3,5-bis(trifluoromethyl)benzene) (M = Ir (**D3**); Rh (**D7**)) and $[(\eta^6\text{-arene})RuCl_2]_2$ (**D8−D10**) were prepared by the reported methods[40,41,52−58] or using the modified procedure (**D6**; see the Supporting Information). It should be noted that the arene ligand of ruthenium complexes is different from that of iridium and rhodium complexes since the presence of η^6-arene

https://doi.org/10.1021/acs.inorgchem.2c03279
Inorg. Chem. 2022, 61, 20008−20025

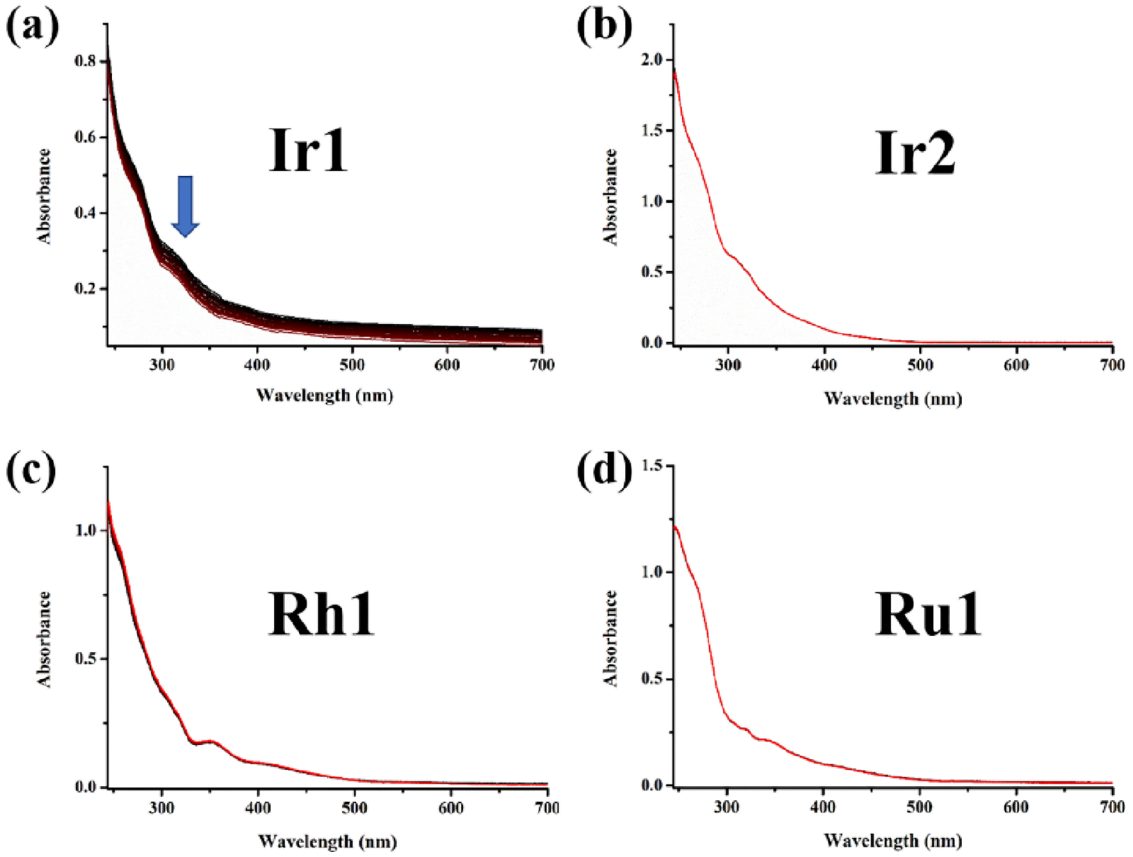

Figure 2. UV−vis spectra for complexes **Ir1**, **Ir2**, **Rh1**, and **Ru1** recorded over a period of 24 h at 37 °C, (a) solution in 25% DMSO/75% PBS (v/v) of **Ir1**; (b) solution in 20% DMSO/80% PBS (v/v) of **Ir2**; (c) solution in 25% DMSO/75% PBS (v/v) of **Rh1**; and (d) solution in 20% DMSO/80% PBS (v/v) of **Ru1**.

substituent was identified to stabilize ruthenium complexes in the +2 oxidation state by being relatively inert to displacement.[59−62] Moreover, another motivation for the development of air-stable η^6-arene ruthenium(II) complexes was the activation by reduction hypothesis, which suggested that active ruthenium(II) species may be formed in vivo from ruthenium(III) complexes.[63−65] Scheme 3 shows the synthetic procedure of zwitterionic phosphine−imine half-sandwich iridium(III), rhodium(III), and ruthenium(II) complexes containing sulfonate moiety. Treatment of precursors **D1**−**D10** with the ligand **L** in methanol for 72 h afforded the complexes **Ir1**−**Ir4**, **Rh1**−**Rh3**, and **Ru1**−**Ru3** in 58−69% isolated yields. These complexes were fairly stable in air and soluble in methanol, dichloromethane, and DMSO. All of the desired compounds were first reported and determined by ^{1}H, ^{13}C{^{1}H}, and ^{31}P{^{1}H} NMR (Figures S6−S35), mass spectrum (ESI, Figures S37−S46), and elementary analyses (C, H, N). The ^{1}H NMR spectra of these complexes showed the characteristic peaks of the Cp^R/arene ring and the *P*,*N*-chelating ligands. Compared to the spectra of the free ligand **L**, the chemical shift of C*H*═N peaks for these complexes changed and appeared at ca. δ 8.58−8.80 ppm, which supported the ligand coordination to the metal center. The splitting of the ^{31}P signal was observed in the ^{13}P{^{1}H} spectrum of the complexes **Rh1**, **Rh2**, and **Rh3**, which was attributed to rhodium−phosphine coupling. The ^{13}C{^{1}H} NMR spectra for these complexes showed the signals of CH═N in the range of δ 175−176 ppm, which appeared more downfield than that (161 ppm) in the free ligand **L**. Further, the molecular structure of some typical complexes was also confirmed by the X-ray crystallography (Figure 1 and Tables S1−S3).

The single-crystal samples of **Ir1**, **Ir2**, and **Rh2** were obtained by the slow diffusion of n-hexane (or a mixture of diethyl ether and n-hexane) into its solution in dichloromethane (or acetonitrile) at room temperature. The selected bond lengths, bond angles, and the crystalline structure of complexes **Ir1**, **Ir2**, and **Rh2** are given in Figure 1. **Ir1**, **Ir2**, and **Rh2** adopted a pseudo-octahedral "three-legged piano-stool" geometry configuration. The "seat" was composed of the Cp^R ring. Moreover, sulfonated phosphine−imine ligand and chloride occupied the three legs in a "piano-stool" configuration. Furthermore, the central metallic iridium(III) or rhodium(III) ion is a portion of a six-membered metallacycle system. The Ir1−Cl1 or Rh1−Cl1 distances of **Ir1**, **Ir2**, and **Rh2** are 2.360(6), 2.409(2), and 2.4292(7) Å, respectively. The Ir1−Cp*(centroid) distances of **Ir2** (1.8448 Å) are slightly shorter than those of **Ir1** (2.0144 Å). The Ir1−P1 or Rh1−P1 bond distances (**Ir1**: 2.260(6) Å; **Ir2**: 2.280(3) Å; **Rh2**: 2.3128(7) Å) of **Ir1**, **Ir2**, and **Rh2** are longer than Ir1−N1 or Rh1−N1 bond distances (**Ir1**: 2.06(2) Å; **Ir2**: 2.132(8) Å; **Rh2**: 2.181(2) Å). Clearly, the cationic centers Ir(III) and Rh(III) are bounded covalently through the phosphine−imine ligand to the terminational negative sulfonate moiety. Hence, the zwitterionic structure of these complexes was successfully identified.

2.2. Stability in Solution. It is meaningful to assess the stability of the metal complexes in aqueous media or physiological conditions for drug development. The hydrolysis

https://doi.org/10.1021/acs.inorgchem.2c03279
Inorg. Chem. 2022, 61, 20008−20025

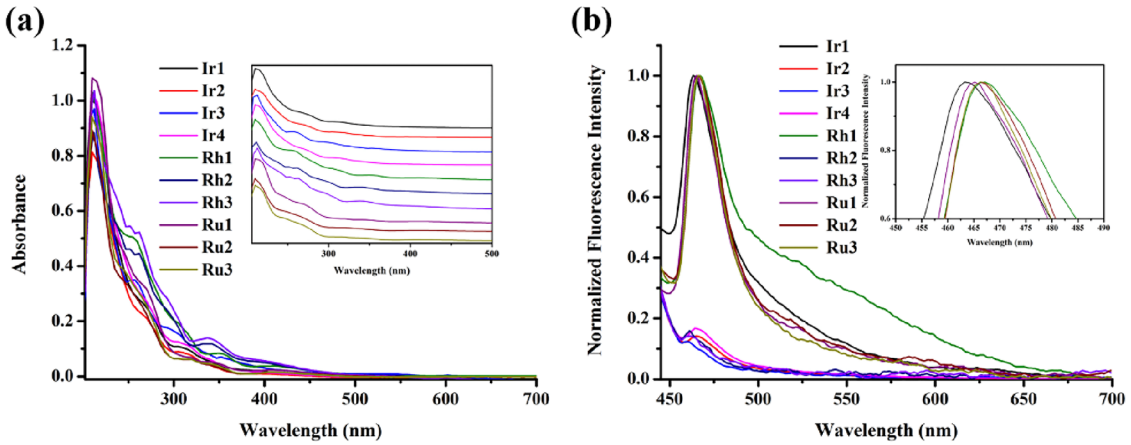

Figure 3. (a) UV/vis spectra of complexes **Ir1**−**Ir4**, **Rh1**−**Rh3**, and **Ru1**−**Ru3** (20 μM) in methanol solutions at 37 °C. The inset represents the offset spectra for clarity. (b) Normalized emission spectra of complexes **Ir1**−**Ir4**, **Rh1**−**Rh3**, and **Ru1**−**Ru3** (20 μM) in methanol at 37 °C (λ_{ex} = 404−407 nm; λ_{em} = 460−466 nm). The inset represents the locally enlarged spectra for clarity. Inset: wavelength from 450 to 490 nm.

of M−Cl bonds, i.e., the exchange of Cl/H_2O, generally represented an important activation step for some transition-metal-based anticancer complexes since M-OH_2 aqua complexes were often more active than the corresponding chloride complexes.[33,66] The stability of these complexes had been assessed in a 20% DMSO/80% PBS (pH ≈ 7.2, prepared from H_2O) (v/v) or 25% DMSO/75% PBS (v/v) using UV−vis spectroscopy at 37 °C at different time intervals (Figures 2 and S47). Minor changes of absorption intensities were detected in the spectrum of complex **Ir1** for a period of 8 h (Figure 2a). However, only negligible changes were found in the absorption spectra of complexes **Ir2**−**Ir4**, **Rh1**−**Rh3**, and **Ru1**−**Ru3**, which suggested their sufficient stability in aqueous solutions (e.g., **Ir2** in Figure 2b). It seemed that the change in the metal center from Ir(III) to Rh(III) increased their stability (**Ir1** vs **Rh1**). Further, the stability of several typical zwitterionic phosphine−imine complexes (**Ir1**, **Rh1**, and **Ru1**) in 90% DMSO-d_6/10% PBS (pH ≈ 7.2, prepared from D_2O) (v/v) or 85% DMSO-d_6/15% PBS (v/v) was also monitored through ^{1}H NMR spectroscopy (Figures S48−S50). The spectra data of the above-mentioned complexes under the test conditions presented no changes over time at 37 °C, evidencing that no hydrolysis occurred in the concentrated solutions. Additionally, the NMR analysis of these complexes was in agreement with their corresponding molecular structure over 24 h, indicating that no ligand dissociation and decomposition occurred under the experimental conditions. The stability of these complexes in pure DMSO was also evaluated. The ^{1}H NMR spectra of **Ir1** exhibited no obvious change over 24 h, and the assignment of protons was completely in agreement with its molecular structure (Figure S51), suggesting that this type of zwitterionic complex showed sufficient stability in DMSO. Overall, the experiments demonstrated that these zwitterionic complexes were fairly stable and could be subjected to perform further biological studies under physiological conditions. Notably, our previously reported zwitterionic pyridyl−imine *N*,*N*-chelating iridium(III) or ruthenium(II) complexes also demonstrated good aqueous stability.[35]

2.3. Spectroscopic Studies. The UV−visible absorbance spectra of complexes **Ir1**−**Ir4**, **Rh1**−**Rh3**, and **Ru1**−**Ru3** in methanol solutions at 37 °C are shown in Figure 3a. The maximum of a sharp band appeared at ca. 210 nm for all of the complexes. In addition, two weak and broad bands maximum at ca. 260 and 350 nm were observed, respectively. The absorption bands below 350 nm were attributed to spin-allowed π−π* ligand-centered transitions. The wide and low-intensity bands at ca. 410 nm were detected in these complexes, which was considered to be related to spin-allowed charge transfer from metal to ligand (MLCT) since the peak above 350 nm could not be found in the absorption spectra of the free ligand.

Upon excitation at 404−407 nm, **Ir1**−**Ir4**, **Rh1**−**Rh3**, and **Ru1**−**Ru3** exhibited blue emissions with maxima at 460−466 nm (**Ir1**: 463 nm, **Ir2**: 465 nm, **Ir3**: 460 nm, **Ir4**: 464 nm, **Rh1**: 465 nm, **Rh2**: 461 nm, **Rh3**: 461 nm, **Ru1**: 464 nm, **Ru2**: 466 nm, **Ru3**: 466 nm) at 37 °C in methanol (Figure 3b). They showed similar emission spectra, indicating that the variation of the Cp^R/arene ring and the metal center has a minor influence on the spectral emission bands. The emission quantum yields (Φ) of the representative complexes **Ir1**, **Rh1**, and **Ru1** were determined, respectively, with a calibrated integrating sphere system. The absolute quantum yields of these complexes are in the order **Rh1** (0.26) > **Ru1** (0.18) > **Ir1** (0.14). Further, the average lifetimes of **Ir1**, **Rh1**, and **Ru1** are 4.61, 4.27, and 4.50 μs, respectively (Figure S52), indicating that these complexes are fluorescent. The photoluminescent characteristic could make it possible to investigate the mechanism of actions of the complexes by bioimaging.

2.4. Cytotoxicity. With cisplatin and half-sandwich complex RAPTA-C as control, the cytotoxicity of **Ir1**−**Ir4**, **Rh1**−**Rh3**, and **Ru1**−**Ru3** toward lung cancer A549 cells and cervical carcinoma HeLa cells was determined using MTT assay (Table 1). Notably, no cytotoxicity (IC_{50} > 100 μM, IC_{50}: half-maximal inhibitory concentration) was observed by the free ligand (**L**) and dimer precursors (**D1**−**D10**) (Table S4), suggesting that the cytotoxicity of the complexes in this system was ascribed to the chelation. Notably, these zwitterionic phosphine−imine iridium(III) complexes **Ir1**−**Ir4** exhibited a significant increase in cytotoxic behaviors than our previously reported zwitterionic pyridyl−imine iridium(III) complexes against all of the tested cancer cell lines, which have been shown to be inactive (e.g., Figure 4, **Ir1** vs **A**).[40,41] Moreover, the zwitterionic *P*,*N*-chelating iridium(III) complexes also showed higher cytotoxicity than the fluorinated zwitterionic *N*,*N*-chelating iridium(III) complexes (Figure 4, **Ir1** vs **B**).[41] Similarly, the title ruthenium(II) complexes

https://doi.org/10.1021/acs.inorgchem.2c03279
Inorg. Chem. 2022, 61, 20008−20025

Table 1. IC_{50} Values of Complexes Ir1−Ir4, Rh1−Rh3, and Ru1−Ru3 Tested toward Cancer and Normal Cell Lines and Comparison with Cisplatin and RAPTA-C

	IC_{50} (μM)		
complex	A549	HeLa	BEAS-2B
Ir1	14.7 ± 0.4	9.1 ± 0.2	25.3 ± 0.6
Ir2	15.6 ± 0.1	8.0 ± 0.1	27.6 ± 0.1
Ir3	15.2 ± 0.1	8.5 ± 0.4	25.6 ± 0.2
Ir4	16.1 ± 0.2	7.2 ± 0.7	29.3 ± 0.3
Rh1	21.1 ± 0.6	10.3 ± 1.1	35.3 ± 0.1
Rh2	23.1 ± 0.2	9.5 ± 0.8	34.7 ± 1.2
Rh3	22.6 ± 0.5	12.2 ± 0.3	35.7 ± 0.9
Ru1	88.2 ± 0.3	81.5 ± 0.1	93.3 ± 0.3
Ru2	90.9 ± 0.1	79.6 ± 0.2	98.3 ± 0.3
Ru3	121.3 ± 0.4	98.6 ± 0.5	115.5 ± 0.4
Cisplatin	21.3 ± 1.7	7.5 ± 0.2	42.0 ± 2.3
RAPTA-C	>150	87.1 ± 0.3	>150

showed the improvement in the cytotoxicity compared with the inactive zwitterionic *N*,*N*-chelating ruthenium(II) complexes (Figure 4, **Ru2** vs **C**).[67] Moreover, the cytotoxicity of these ruthenium(II) complexes toward HeLa and A549 cells was comparable to or even higher than the reference half-sandwich phosphine ligation complex RAPTA-C. The zwitterionic phosphine−imine rhodium(III) complex also displayed the cytotoxicity comparable to the cisplatin (Figure 4, **Rh1**). Obviously, the introduction of phosphine into zwitterionic complexes could significantly increase the cytotoxic potency. Previous studies have shown that the lack of cytotoxicity of zwitterionic pyridyl−imine iridium(III) and ruthenium(II) complexes appeared to arise from their low lipophilic property and the lipophilic fluorinated substituents could increase their anticancer activity.[40,41] This prompted us to investigate the lipophilicity of these novel zwitterionic phosphine−imine complexes. The log *P* values (partition coefficients between octanol and water) for the above-mentioned complexes were measured through a general "shake flask" method. The trend in lipophilicity has been revealed using the log *P* values as follows: **Ir1** (2.19) > **Rh1** (1.44) > **Ru1** (1.28) > **Ru2** (1.02) > **Ru3** (0.78). The log *P* values of the zwitterionic phosphine−imine iridium(III) and ruthenium(II) complexes were significantly higher than those of the corresponding zwitterionic pyridyl−imine iridium(III) and ruthenium(II) complexes (log *P* values: Figure 4, **Ir1** (2.19) vs **A** (0.26) and **B** (1.43); **Ru1** (1.28), **Ru2** (1.02) and **Ru3** (0.78) vs **C** (−0.71)).[40,41,67] Clearly, compared with zwitterionic pyridyl−imine iridium(III) and ruthenium(II) complexes, the lipophilicity of zwitterionic phosphine−imine iridium(III) and ruthenium(II) complexes greatly increased. Thus, the strategic incorporation of phosphine into zwitterionic complexes could increase their lipophilicity. Meanwhile, the introduction of lipophilic phenyl rings adjacent to phosphine (PPh_2) may also contribute to the enhanced lipophilicity of these zwitterionic complexes. In general, cell uptake and cytotoxicity were correlated with lipophilicity. Therefore, the total cell uptake accumulation of some zwitterionic complexes was tested using inductively coupled plasma-mass spectrometry (ICP-MS) by exposure to these complexes (5 μM) for 48 h. The intracellular contents (ng/μg protein) are as follows: **Ir1** (0.653) > **Rh1** (0.622) > **Ru2** (0.325) > **Ru1** (0.311) > **Ru3** (0.267). The order of level of cell uptake was basically consistent with the above-mentioned lipophilicity and their cytotoxic activity. As a result, it seemed that the increased lipophilic property and cellular uptake of these zwitterionic phosphine−imine half-sandwich complexes were likely to be one of the key factors of their enhanced cytotoxicity. The modifications of substituents on the η^5-Cp^R ring have little influence on the cytotoxic activity (**Ir1** vs **Ir2** vs **Ir3** vs **Ir4**). In particular, the presence of lipophilic fluorinated substituents in the η^5-Cp^R did not result in a significant increase in cytotoxicity (**Ir3** vs **Ir1**, **Ir2** and **Ir4**; **Rh3** vs **Rh1**

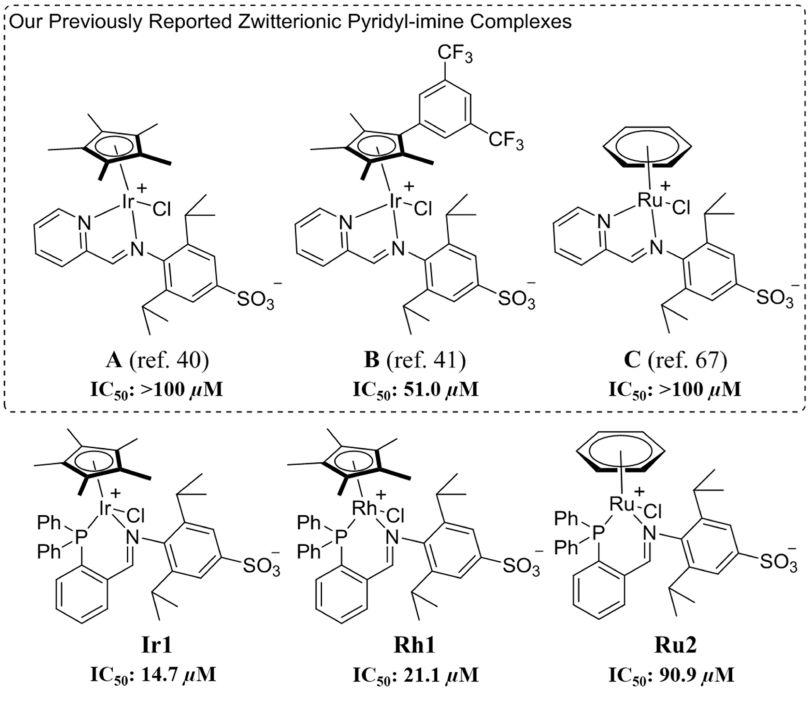

Figure 4. IC_{50} values of previously reported complexes and the title complexes in this work toward A549 cells.

https://doi.org/10.1021/acs.inorgchem.2c03279
Inorg. Chem. 2022, 61, 20008−20025

and **Rh2**), which is different from the tendency of our previously reported zwitterionic pyridyl−imine system.[41] The major role of the phosphine ligation may have offset the advantages of having the fluorinated phenyl rings in the zwitterionic phosphine−imine system. The iridium(III) and rhodium(III) complexes exhibited higher cytotoxicity than the corresponding ruthenium(II) complexes, suggesting that the metal center has a significant effect on the cytotoxicity of these complexes. As mentioned above, ruthenium(II) complexes with η^6-arene ligands in this system gave rise to a decreased hydrophobicity compared to η^5-Cp^R iridium(III) and rhodium(III) complexes, thus leading to a decreased cell uptake and cytotoxicity. The cytotoxic action of **Ir1**−**Ir4**, **Rh1**−**Rh3**, and **Ru1**−**Ru3** against the noncancerous BEAS-2B has also been investigated. Unfortunately, there was no obvious selectivity for normal and cancer cells. **Ir1** showed the highest cytotoxicity against A549 cells, and thus it was selected for further investigations of MoAs.

2.5. DNA Binding Results. Binding to DNA was relevant to the cytotoxic activity of antitumor agent since DNA was considered the most potential target site for metal-based antitumor complexes.[68] The time-dependent ^{1}H NMR spectra of **Ir1**, **Rh1**, or **Ru1** mixed with the model nucleobase 9-methyladenine (9-MeA) in 90% DMSO-d_6/10% D_2O or 85% DMSO-d_6/15% D_2O solutions at 37 °C were utilized to detect the coordination of 9-MeA with **Ir1**, **Rh1**, or **Ru1** (Figures S53−S55). There was no coordination reaction occurring with 9-MeA at various time intervals within 24 h. Moreover, the result of mass spectrum also showed that no nucleobase adduct of these complexes was generated.

Further, the interaction between complexes **Ir1**, **Rh1**, and **Ru1** and CT-DNA was monitored via UV−vis absorption spectroscopy (Figures 5 and S1). With the fixed concentration

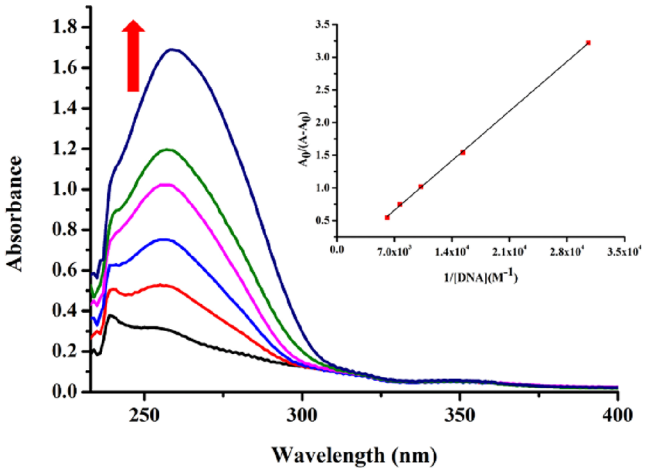

Figure 5. UV−vis titration spectra of **Rh1** complexes (60 μM) in 5 mM tris−HCl/10 mM NaCl buffer solution (pH = 7.2) with increasing concentration of CT-DNA (0−163.4 μM). (Inset) Plots of $A_0/(A - A_0)$ vs 1/[DNA].

of these complexes, CT-DNA solution was added regularly. As shown in Figure 5, the hyperchromism and red shift (ca. 1.5 nm) were observed for **Rh1** in a slow increase of CT-DNA concentration, suggesting noncovalent binding modes of electrostatic binding.[69−71] Also, the Benesi−Hildebrand equation is solved numerically to calculate the binding constants (K_b). The calculated K_b values for the above-mentioned complexes ranged from 9.06×10^2 to 3.02×10^3 M^{-1} (**Ru1**: $K_b = 3.020 \times 10^3$ M^{-1}, **Ir1**: $K_b = 1.427 \times 10^3$ M^{-1}, **Rh1**: $K_b = 9.062 \times 10^2$ M^{-1}), showing that the binding efficacy to CT-DNA was not significant for these complexes. These results suggested that these complexes displayed a weak interaction with CT-DNA and it seemed not to be the major MoAs for these zwitterionic phosphine−imine complexes.

2.6. Protein Binding Studies. The serum albumin usually plays a major role in transportation and metabolism of drugs in cancer cells.[72] BSA (bovine serum albumin) serving as a target protein is commonly used to study the binding of drugs with plasma proteins on account of the structural similarity to HSA (human serum albumin). Herein, the binding potency of **Ir1**, **Rh1**, and **Ru1** with BSA could be assessed using UV−vis absorption spectrum and fluorescence spectrum (Figure 6). UV−vis absorption spectra of BSA were observed before and after the addition of complexes (Figure 6a−c). The absorbance effect of complexes could be eliminated by adding drug solutions in the same concentration to the reference cells. The intensities of the absorption peak at 229 nm regularly decreased and red-shifted (229−233 nm) with the increased concentration of the drugs, which can be attributed to induce α-helix perturbation and the role of ambient polarity.[73−76] In addition, at the weak absorption peak at ca. 276 nm, a subtle increase in the intensity and hardly any shift for the absorbance peak position were observed, suggesting a kind of tiny variation of microenvironment of aromatic amino acid residues (Phe, Tyr, and Trp) in BSA.[75−79]

Moreover, the interaction between the sample and BSA could be further investigated by studying the fluorescence quenching of BSA as the concentration of the drugs increased at room temperature. The correction for the inner filter effect was applied to calibrate the measured fluorescence.[80] In general, the fluorescent characteristic of BSA is mainly due to two residues of the protein named tryptophan and tyrosine. The release of fluorescence arising from aromatic amino acid residues was much sensitive to microenvironmental variety. Therefore, the fluorescence emission could be attenuated by binding small-molecule complexes near the residues.[75] The increasing concentration of the complexes led to a regular decline in the fluorescence intensity of the BSA at ca. 350 nm, which could be attributed to the static quenching mechanism after the complexes bound to the protein. The values of K_{sv}, K_q, K_b, and n could be obtained using the conventional Stern−Volmer equation and Scatchard equation in a static quenching process (Table 2).[81,82] The calculated value of K_q for **Ir1** was 5.39×10^{12} M^{-1} s^{-1}, which was hundreds of times greater than that of the dynamic type of quenching (2.0×10^{10} M^{-1} s^{-1}), further indicating that these complexes could bind to BSA mainly through static quenching process. The calculated value of K_b of **Ir1** and **Rh1** reached the order of 10^4 M^{-1}, suggesting intense binding to BSA. Notably, the calculated value of K_b of **Ru1** was 1 order of magnitude smaller than that of **Ir1** and **Rh1**, which might be associated with the low anticancer activity of ruthenium complexes. In addition, the number of binding sites (n) in BSA approximates 1.0 for **Ir1**, **Rh1**, and **Ru1**, showing that only one site in BSA reacted with the corresponding complexes.

Synchronous fluorescence spectroscopy was also monitored to further clarify the conformational changes that occurred to BSA after adding complexes (Figures S56 and S57). The spectra of tryptophan residues (Trp) and tyrosine residues (Tyr) were given. With an incremental addition of typical

https://doi.org/10.1021/acs.inorgchem.2c03279
Inorg. Chem. 2022, 61, 20008−20025

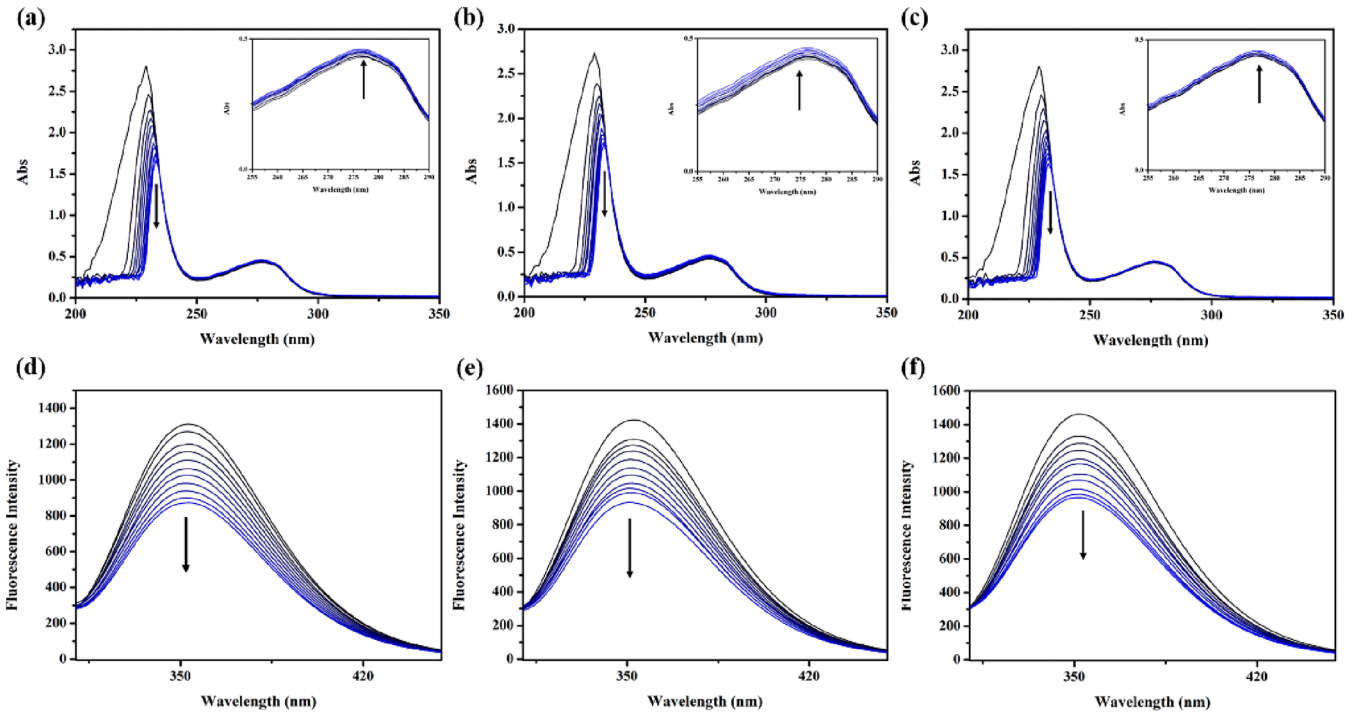

Figure 6. UV−vis spectrum of BSA (10 μM) in 5 mM tris−HCl/10 mM NaCl buffer solution (pH = 7.2) upon addition of the complex (a) **Ir1**, (b) **Rh1**, and (c) **Ru1** (0−10 μM). Inset: wavelength from 255 to 290 nm. Fluorescence spectra of BSA (10 μM; λ_{ex} = 288 nm; λ_{em} = 350 nm) in the absence and presence of the complexes (d) **Ir1**, (e) **Rh1**, and (f) **Ru1** (0−10 μM). The arrow shows the intensity changes when the concentration of the iridium(III), rhodium(III), or ruthenium(II) complex increases.

Table 2. Quenching Parameters and Binding Parameters for the Interaction of Complexes Ir1, Rh1, and Ru1 with BSA

complex	k_{sv} (10^4 M^{-1})	K_q (10^{12} M^{-1} s^{-1})	K_b (10^4 M^{-1})	n
Ir1	5.39 ± 0.06	5.39	1.43	0.874
Rh1	5.82 ± 0.29	5.82	1.38	0.868
Ru1	4.96 ± 0.12	4.96	0.21	0.707

complexes, the fluorescence intensities corresponding to both Trp ($\Delta\lambda$ = 60, 286 nm) and Tyr ($\Delta\lambda$ = 15, 291 nm) decreased and a 1−2 nm red shift occurred to tryptophan at the maximum emission wavelength. Overall, these results have established that the introduction of the title complexes altered the conformation of BSA, decreased the microenvironmental hydrophobicity of the tryptophan residues, and enhanced the extension degree of the BSA macromolecule peptide chain.

2.7. ROS Determination. Highly oxidizing drugs could produce reactive oxygen species (ROS) to induce cell oxidative death. The ROS assay kit was used to determine the generation of ROS in A549 cells induced by **Ir1** (Figures 7 and S58). Compared to control cells, the obvious concentration-dependent increase in ROS levels was observed in the treated A549 cells, indicating that complex **Ir1** could result in the accumulation of intracellular ROS. It has been reported that the potency of anticancer agents to induce apoptosis was associated with the potency of generating ROS in cancer cell lines. Thus, the induction of cell apoptosis was also studied in the next experiment.

2.8. Apoptosis and Cell Cycle Studies. One of the potential goals of treating anticancer agents is targeting cancerous cells and inducing cell death by apoptotic pathways. The annexin V/PI technique was used to reveal apoptotic cell death. **Ir1** was continuously incubated with lung cancer A549

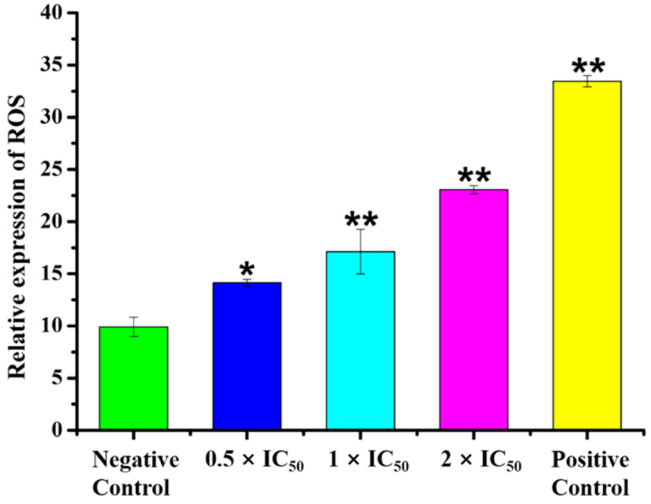

Figure 7. Analysis of ROS levels by fluorescence microscope after A549 cells were treated with **Ir1** for 24 h at 37 °C and stained with DCFH-DA. *P* values were calculated after a *t* test against the negative control data, *p < 0.05, **p < 0.01.

cells for up to 48 h, and then the treated cells were examined using flow cytometry. The proportion of early apoptosis increased after treatment with **Ir1** (Figure 8 and Table S5). Hence, the exposure to these zwitterionic phosphine−imine complexes could induce apoptosis and accordingly lead to cancer cell death.

To demonstrate whether the induction of apoptosis was the primary pathway for the cancer cell death, the cytotoxicity of **Ir1** was determined in the presence of various inhibitors including autophagy inhibitor 3-methyladenine (3-MA), necroptosis inhibitor necrostatin-1 (Nec-1), the protease

https://doi.org/10.1021/acs.inorgchem.2c03279
Inorg. Chem. 2022, 61, 20008−20025

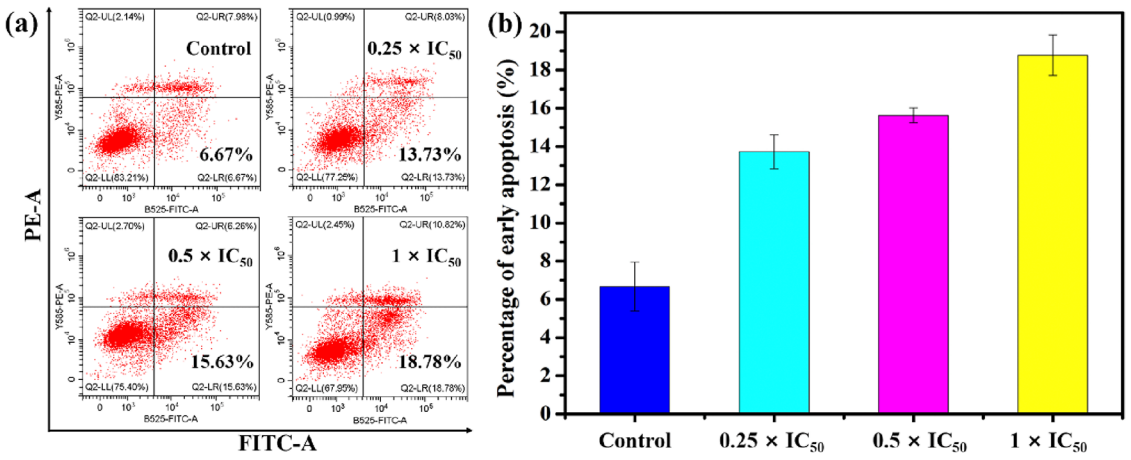

Figure 8. (a) Apoptosis analysis of A549 cells after 48 h of exposure to complex **Ir1** at 37 °C determined by flow cytometry using annexin V-FITC vs PI staining. (b) Histograms of early apoptosis analysis for A549 cells after treated with complex **Ir1** (0.25 × IC_{50}, 0.5 × IC_{50} and 1 × IC_{50}) for 48 h. Data are quoted as mean ± SD of three replicates.

inhibitor leupeptin (LPT), and the protein synthesis inhibitor cycloheximide (CHX) (Table S6). The negligible changes were observed in the cytotoxic efficacy, indicating that these inhibitors were inoperative and apoptosis was the primary pathway for cancer cell death.

To investigate the role of zwitterionic phosphine−imine complexes in cell cycle arrest, the flow cytometry was also used to analyze the blocking of cell cycle progression by **Ir1** (Figure S59). The results showed that G0/G1, S, and G2/M phases had a trivial change in A549 cells at the concentrations of 0.25, 0.5, and 1 × IC_{50}. Therefore, these complexes seemed not to effectively disrupt the cell cycle progression.

2.9. Cellular Uptake Mechanisms. Based on the consideration of the fluorescence properties of the above-mentioned products, the intracellular uptake principle of the most active **Ir1** could be detected by laser confocal microscopy. Energy-dependent and energy-independent pathways are two kinds of ways for small-molecule complexes to enter cells.[83] As Figure 9 illustrates, the appearance of punctate green fluorescence indicated that **Ir1** entered into A549 cells after a 1 h incubation. A marked decline of fluorescence strength was observed at the time when A549 cells were incubated with **Ir1** under 4 °C or CCCP conditions (CCCP: carbonyl cyanide 3-chloro-phenylhydrazone, a kind of metabolic inhibitor), in comparison with the control group of 37 °C (Figure 9). These results suggested that the cellular uptake of complex **Ir1** is energy-dependent. In addition, there was a negligible change in intracellular fluorescence intensity after treatment with chloroquine (a kind of endocytosis inhibitor) compared to that of the untreated group (Figure 9), indicating that endocytosis was not involved in the cellular uptake.

Antimycin A_1, which played a role in lowering ATP levels, was used to coincubate with complex **Ir1** to further validate the energy-dependent cellular uptake mechanisms (Figure 10a). The experimental results showed that the accumulation of iridium in A549 cells was affected after the changes of ATP levels, which was consistent with the observation of significant cellular uptake at relatively high temperatures (Figure 10a and Table S7; 37 °C vs 4 °C).

Moreover, the means of protein-mediated uptake were also investigated. Amphotericin B could disrupt cell membrane integrity to form pores, which may lead to increased cell

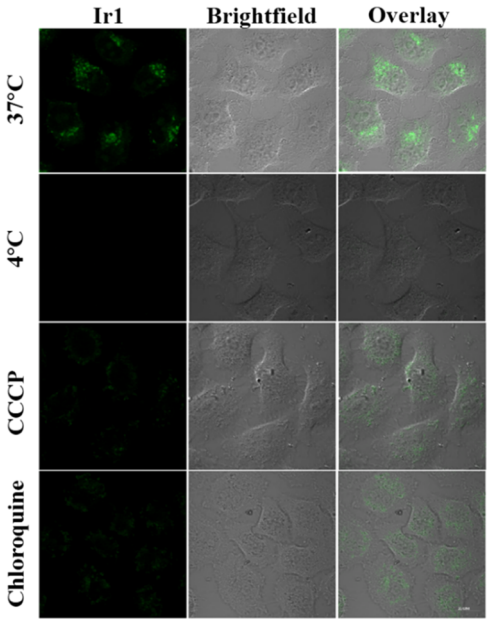

Figure 9. Effects of temperatures (37 or 4 °C), chloroquine (50 μM), and CCCP (50 μM) on the cellular uptake of **Ir1** (2 μM). Scale bar: 20 μm, λ_{ex} = 405 nm, λ_{em} = 430−490 nm.

accumulation. A549 cells and complex **Ir1** were cotreated with variable concentrations of amphotericin B. The level of cell accumulation of iridium exhibited no significant variation (Figure 10b and Table S8), suggesting that facilitated diffusion (an energy-independent pathway) was not responsible for the uptake pathway of complex **Ir1**.

2.10. Cellular Localization. Whether these complexes were able to target organelles was further assessed by the cellular localization analysis via confocal microscopy (Figure 11). The A549 cells were dual-stained with **Ir1** and nucleus fluorescent probe (4,6-diamino-2-phenyl indole, DAPI), mitochondrial fluorescent probe (Mito Tracker Red CMH2XRos, MTDR), and lysosome fluorescent probe (LysoTracker Red DND-99, LTDR). In the cytoplasm, the punctate and intense green fluorescence showed that **Ir1** could effectively penetrate A549 cells after a 1 h incubation. The degree of mergence between **Ir1** and DAPI or MTDR was

https://doi.org/10.1021/acs.inorgchem.2c03279
Inorg. Chem. 2022, 61, 20008−20025

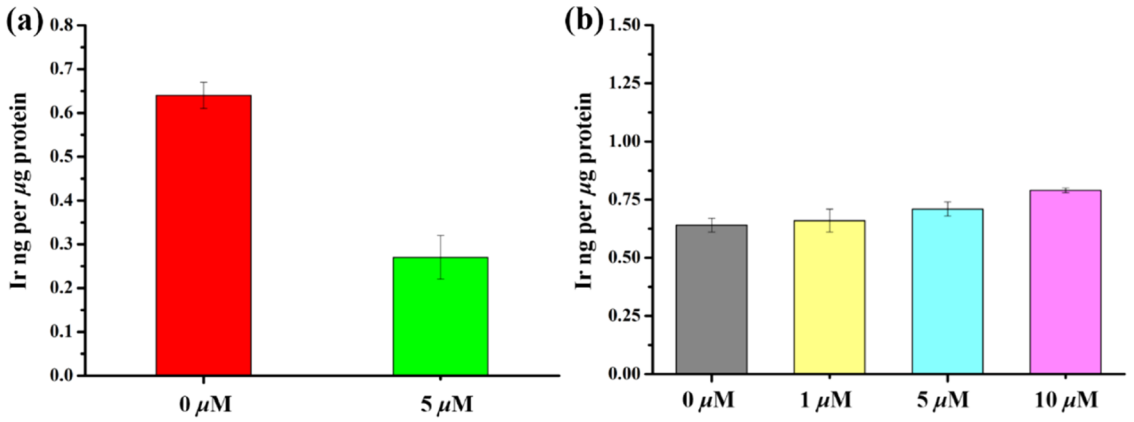

Figure 10. Total accumulation of Ir in A549 cells when coincubated with complex **Ir1** (5 μM) and (a) antimycin A_1 (0 and 5 μM) or (b) amphotericin B (0, 1, 5 and 10 μM) after exposure to **Ir1** for 48 h at 37 °C with no recovery time.

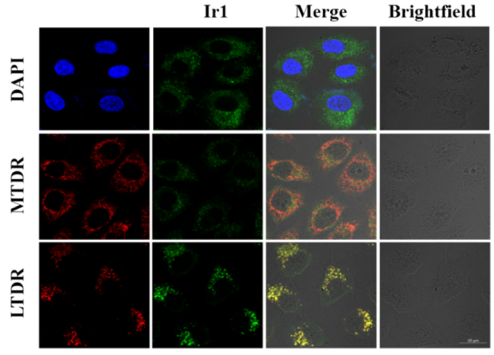

Figure 11. Determination of the intercellular localization of **Ir1** by confocal microscopy. A549 cells were incubated with **Ir1** (2 μM) for 1 h at 37 °C and then coincubated with DAPI (1 μg/mL), MTDR (500 nM), or LTDR (75 nM) for 1 h (**Ir1**, λ_{ex} = 405 nm, λ_{em} = 460−520 nm; DAPI, λ_{ex} = 345 nm, λ_{em} = 410−455 nm; MTDR, λ_{ex} = 644 nm, λ_{em} = 660−720 nm; LTDR, λ_{ex} = 594 nm, λ_{em} = 600−660 nm). Scale bar: 20 μm. The green, red, and blue fluorescence represent **Ir1**, mitochondria or lysosome, and nucleus, respectively.

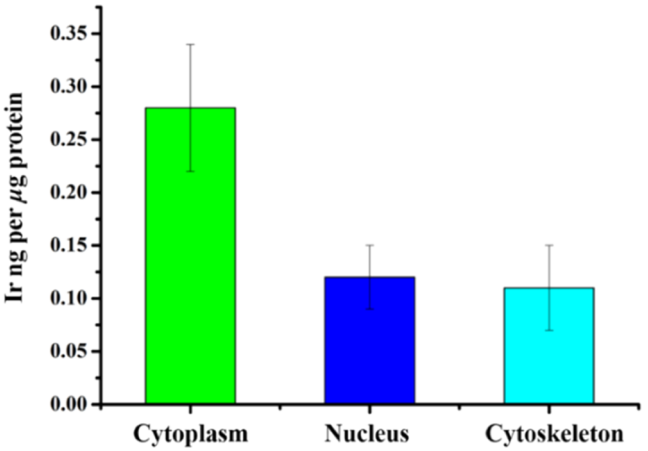

Figure 12. Iridium content of the cytoplasm, nucleus, and cytoskeleton fractions (Ir ng per μg protein) of A549 cells after 48 h of exposure to 5 μM **Ir1**.

negligible with a low Pearson correlation coefficient (PCC) value (DAPI: PCC = 0.11; MTDR: PCC = −0.04), indicating that **Ir1** cannot effectively localize in the nucleus and mitochondria. The weak binding efficacy of these complexes to CT-DNA (see above; the low K_b value in Section 2.5) may be associated with the low accumulation in the nucleus. However, the concordance with a PCC value of 0.78 was found between the merged image of **Ir1** and LTDR, suggesting that **Ir1** primarily targeted lysosome. Thus, lysosome-mediated cell death could be responsible for the cytotoxic potency of these zwitterionic phosphine−imine complexes. Possibly, the high lipophilicity of these zwitterionic *P,N*-chelating complexes may be related to the lysosome targeting. However, the previous study has shown that lysosome accumulation and targeting are associated with various factors including lipophilicity, type and number of charges of complexes, aromatic area, and charge/mass ratio.[84−90]

The biodistribution in different subcellular compartments of the A549 cells was also quantitatively studied by ICP-MS. After 48 h of exposure to **Ir1**, the iridium content of the cytoplasm, nucleus, and cytoskeleton fractions isolated from A549 cells was determined (Figure 12 and Table S9). As shown in Figure 12, the highest concentration of iridium was in the cytoplasm section and more iridium entered the cytoplasm than the nucleus. These results are consistent with the above-mentioned observations of cellular localization experiments.

2.11. Lysosomal Damage. The functional state of lysosomes could be monitored by acridine orange (AO), which was a kind of probe of lysosome dysfunction with red or green photoluminescence in lysosomes or in the cytosol and nuclei.[91] Hence, the lysosome integrity could be further investigated by AO to study cell death pathway mediated by lysosomes. As shown in Figure 13, A549 cells stained with AO have strong red photoluminescence in lysosomes. However, the intensity of red photoluminescence showed a significant decrease with the increased concentration of **Ir1**, indicating that lysosomal integrity was damaged after the treatment of **Ir1**. Since the disruption of lysosomal integrity could result in the release of cathepsin B from the lysosomes into the cytosol, lysosomal damage was further determined by the fluorogenic magic red MR-$(RR)_2$ to monitor the intracellular activity of cathepsin B (Figure S60). The control cells exhibited red fluorescence that was predominantly localized in the lysosomes. The red fluorescence gradually spread with the increased concentration of **Ir1**, suggesting that cathepsin B gradually entered into the cytosol from lysosomes. The above-mentioned results further suggested that these zwitterionic phosphine−imine complexes might target lysosomes and thus cause lysosomal damage.

https://doi.org/10.1021/acs.inorgchem.2c03279
Inorg. Chem. 2022, 61, 20008−20025

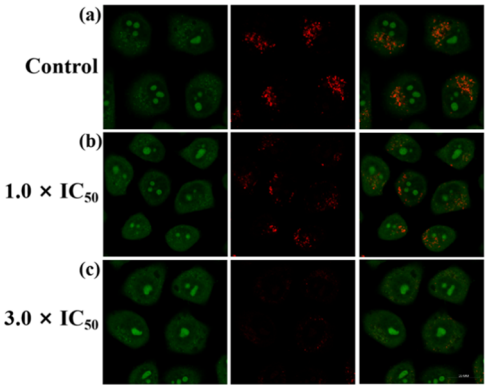

Figure 13. Lysosomal disruption of A549 cells verified with AO assay. (a) Cells only treated with AO, as a control; (b,c) cells treated with AO and **Ir1** (1 and 3 equipotent concentrations of IC_{50}), AO green fluorescence, λ_{ex} = 488 nm and λ_{em} = 510 ± 20 nm; AO red fluorescence, λ_{ex} = 488 nm and λ_{em} = 625 ± 20 nm. Scale bar: 20 μm.

2.12. Inhibition of Cell Migration. Malignant cancer cells tended to metastasize to adjacent or distant tissues due to the reduced superficial adhesion. Herein, the wound-healing assay was conducted to observe the inhibition action of complex **Ir1** on the migration of A549 cells. Compared to 45.3% of the control group, the wound closure rate (WCR) of A549 cells treated with **Ir1** not only significantly decreased to 28.7% at 0.25 × IC_{50} but also presented a concentration-dependent characteristic (Figure 14). This result implied that the complex **Ir1** could inhibit the migration of A549 cells. Consequently, **Ir1** has both pretty good anticancer ability and antimetastatic potential, which might contribute to addressing the issue of advanced malignancy metastasis.

3. CONCLUSIONS

In summary, with an easy access to the sulfonated phosphine−imine ligand, the synthesis and characterization of a family of zwitterionic phosphine−imine half-sandwich iridium(III), rhodium(III), and ruthenium(II) complexes have been presented. These new complexes performed basically stable in aqueous solution and have a detectable photoluminescence. Notably, the presence of phosphine ligation was beneficial for improving the lipophilic properties and cellular uptake effects of these zwitterionic complexes, further affording an enhanced cytotoxic efficacy against A549 and HeLa cell lines. Moreover, the representative complexes exhibited no coordination reaction with 9-MeA, and the weak affinity between these zwitterionic phosphine−imine complexes and CT-DNA was observed. In addition, the spectroscopic analysis supported the binding of the typical complexes to BSA. The mechanistic study showed that the most reactive complex **Ir1** could increase the ROS levels, induce apoptosis, target, and damage lysosomes. Meanwhile, this type of zwitterionic phosphine−imine complex could also suppress cancer cell migration.

4. EXPERIMENTAL SECTION

4.1. General Information. All solvents and reagents were commercially sourced. Unless otherwise stated, they were used without further purification. The sodium 2,6-diisopropylaniline sulfonate and RAPTA-C were prepared using the literature procedure.[92,93] The ^{1}H, ^{13}C{^{1}H}, and ^{31}P{^{1}H} NMR spectroscopy were determined via Bruker DPX 500 spectrometers (Figures S2−S35). And absorption spectroscopy was performed by a TU-1901 UV−visible recording spectrophotometer. MS of these new products was recorded on a Thermo LTQ Orbitrap XL (ESI^{+}; Figures S36−S46). XRD analysis results were collected by a Bruker Apex SMART CCD area detector (Tables S1−S3) with graphite-monochromated Mo Kα radiation. Elemental analysis (C, H, N) was determined by vario El cube.

4.2. Synthesis of L (Sulfonated Phosphine−Imine Ligand). The sodium 2,6-diisopropylaniline sulfonate (1.22 g), HCOOH (ca. 0.30 g of an 88% aqueous solution), and Na_2SO_4 (1.10 g) were added to a solution of 2-(diphenylphosphinyl)benzaldehyde (1.17 g) in CH_2Cl_2 and MeOH (1:1, v/v) mixed solvents (60 mL). The suspension was vigorously stirred at room temperature for 24 h. The mixture was filtered. The filtrate was collected and concentrated under reduced pressure. Recrystallization from MeOH afforded yellow crystals. The yellow crystal was washed using Et_2O under ultrasound, filtered, and dried to obtain **L** as a light-yellow powder.

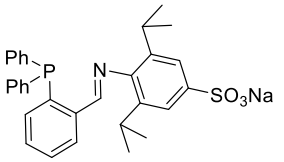

Light-yellow powder, yield: 1.30 g (58.3%). ^{1}H NMR (500 MHz, DMSO-d_6) (ppm): δ 8.72 (d, J = 5.1 Hz, 1H, C*H*═N), 8.21−8.19 (m, 1H), 7.59 (t, J = 7.2 Hz, 1H), 7.52 (t, J = 7.4 Hz, 1H), 7.41 (s, 6H), 7.31 (s, 2H), 7.24−7.14 (m, 4H), 6.88−6.86 (m, 1H), 2.62−2.54 (m, 2H, C*H*(CH$_3$)$_2$), 0.92 (d, J = 6.8 Hz, 12H, CH(C*H*$_3$)$_2$). ^{13}C{^{1}H} NMR (126 MHz, DMSO-d_6) (ppm): δ 161.05 (CH═N), 160.88, 149.28, 144.16, 138.73, 138.59, 138.42, 136.55, 136.47, 136.39, 134.08, 133.92, 133.64, 131.99 129.86, 129.64, 129.39, 129.34, 128.95, 128.92, 120.64, 27.77 (*C*H(CH$_3$)$_2$), 23.61 (CH-(*C*H$_3$)$_2$). ^{31}P{^{1}H} NMR (202 MHz, DMSO-d_6) (ppm): δ 14.84. ESI-

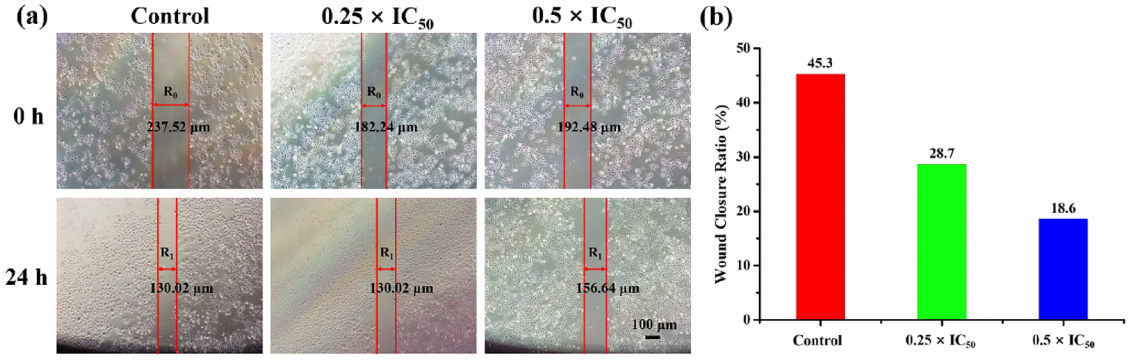

Figure 14. Wound-healing assay of A549 cells treated with **Ir1** for 24 h. (a) Typical images were taken at 0 and 24 h. The widths of the wounds are indicated with the lines (μm). Scale bar: 100 μm. (b) Histograms of wound-healing assay after 24 h. Data are quoted as the mean ± SD of three replicates. Wound closure rate = $(R_0 - R_1)/R_0 \times 100\%$.

https://doi.org/10.1021/acs.inorgchem.2c03279
Inorg. Chem. 2022, 61, 20008−20025

MS (m/z): calcd. for $C_{31}H_{33}NO_3PS$: 530.1924, found: 530.0800, $[M - Na + 2H]^+$; ESI-MS (m/z): calcd. for $C_{31}H_{31}NNa_2O_3PS$ 574.1558, found: 573.9900 $[M + Na]^+$.

4.3. Synthesis of Ir1−Ir4, Rh1−Rh3, and Ru1−Ru3 (Sulfonated Phosphine−Imine Complexes). *4.3.1. Common Method.* Precursors (**D1−D10**) and ligand **L** (2 equiv) were dissolved in MeOH and vigorously stirred for 72 h and monitored by thin-layer chromatography (TLC). Then, the solvent was removed under reduced pressure. The residue was dissolved in CH_2Cl_2 and filtered to remove NaCl. The filtrate was concentrated, and an excess of Et_2O was added. The precipitate was washed using Et_2O, filtered, and dried to afford an orange-yellow/orange-red/orange-brown/brown powder.

4.3.2. Ir1.

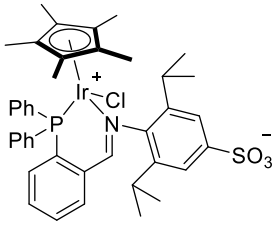

Orange-yellow powder, yield: 69.0 mg (60.9%). ^{1}H NMR (500 MHz, DMSO-d_6) (ppm): δ 8.71 (s, 1H, C*H*═N), 8.00 (s, 1H), 7.82−7.69 (m, 6H), 7.64 (s, 2H), 7.59 (s, 1H), 7.41 (s, 3H), 7.20 (s, 2H), 6.99−6.95 (m, 1H), 3.39−3.35 (m, 1H, C*H*$(CH_3)_2$), 2.08−1.97 (m, 1H, C*H*$(CH_3)_2$), 1.33 (d, J = 6.4 Hz, 3H, CH(C*H*$_3)_2$), 1.15 (s, 15H, Cp^R-C*H*$_3$), 1.05 (d, J = 6.3 Hz, 3H, CH(C*H*$_3)_2$), 1.00 (d, J = 6.3 Hz, 3H, CH(C*H*$_3)_2$), 0.16 (d, J = 6.3 Hz, 3H, CH(C*H*$_3)_2$). ^{13}C{^{1}H} NMR (151 MHz, DMSO-d_6) (ppm): δ 175.25 (*C*H═N), 150.31, 147.99, 143.14, 140.04, 139.15, 137.01, 135.22, 135.15, 134.89, 133.74, 133.07, 132.56, 129.98, 129.91, 129.16, 127.57, 127.19, 127.08, 126.72, 126.11, 125.71, 121.54, 120.69, 119.67, 96.84, 96.83, 92.77, 92.76, 92.17, 27.03 (*C*H$(CH_3)_2$), 26.31 (*C*H$(CH_3)_2$), 25.35 (CH(*C*H$_3)_2$), 25.20 (CH(*C*H$_3)_2$), 22.85 (CH(*C*H$_3)_2$), 22.01 (CH(*C*H$_3)_2$), 8.41 (Cp^R-*C*H$_3$), 8.31 (Cp^R-*C*H$_3$), 8.01 (Cp^R-*C*H$_3$). ^{31}P{^{1}H} NMR (202 MHz, DMSO-d_6) (ppm): δ 6.58. ESI-MS (m/z): calcd. for $C_{41}H_{47}ClIrNO_3PS$ 892.2332, found: 892.2515 $[M + H]^+$; ESI-MS (m/z): calcd. for $C_{41}H_{46}ClIrNNaO_3PS$ 914.2151, found: 914.2290 $[M + Na]^+$. Anal. calcd for $C_{41}H_{46}ClIrNO_3PS$: C, 55.24; H, 5.20; N, 1.57. Found: C, 54.95; H, 5.24; N, 1.65.

4.3.3. Ir2.

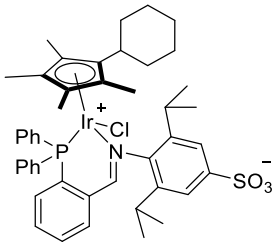

Orange-yellow powder, yield: 140.3 mg (58.3%). ^{1}H NMR (500 MHz, DMSO-d_6) (ppm): δ 8.66 (d, J = 2.6 Hz, 1H, C*H*═N), 8.00−7.98 (m, 1H), 7.80 (t, J = 7.5 Hz, 1H), 7.75−7.72 (m, 5H), 7.65−7.63 (m, 2H), 7.60 (d, J = 1.5 Hz, 1H), 7.58−7.44 (m, 2H), 7.43 (d, J = 1.5 Hz, 1H), 7.29−7.23 (m, 2H), 7.06−7.03 (m, 1H), 3.49−3.41 (m, 2H, C*H*$(CH_3)_2$), 2.10−2.05 (m, 2H, Cy-C*H*$_2$), 1.71−1.68 (m, 2H, Cy-C*H*$_2$), 1.64−1.56 (m, 2H, Cy-C*H*$_2$), 1.46 (s, 3H, Cp^R-C*H*$_3$), 1.41−1.39 (m, 1H, Cy-C*H*$_2$), 1.37−1.34 (m, 6H, Cp^R-C*H*$_3$), 1.30 (d, J = 3.7 Hz, 3H, Cp^R-C*H*$_3$), 1.25−1.23 (d, 1H, Cy-C*H*$_2$), 1.09 (m, 2H, Cy-C*H*$_2$), 1.04 (d, J = 6.5 Hz, 6H, CH(C*H*$_3)_2$), 0.99−0.96 (m, 1H, Cy-C*H*), 0.81 (d, J = 2.6 Hz, 3H, CH(C*H*$_3)_2$), 0.18 (d, J = 6.5 Hz, 3H, CH(C*H*$_3)_2$). ^{13}C{^{1}H} NMR (151 MHz, DMSO-d_6) (ppm): δ 175.94 (CH═N), 150.72, 148.68, 140.57, 139.41, 137.53, 135.44, 134.79, 133.94, 133.84, 133.77, 133.22, 132.83, 130.28, 130.21, 129.66, 129.59, 128.23, 127.85, 127.36, 127.03, 126.99, 126.63, 121.93, 121.25, 107.26, 104.65, 94.39, 94.33, 90.07, 36.79 (Cy-*C*H), 30.26 (Cy-*C*H$_2$), 29.32 (Cy-*C*H$_2$), 27.55 (*C*H$(CH_3)_2$), 26.97 (*C*H$(CH_3)_2$), 26.88 (Cy-*C*H$_2$), 26.66 (Cy-*C*H$_2$), 25.80 (Cy-*C*H$_2$), 25.77 (CH-(*C*H$_3)_2$), 25.54 (CH(*C*H$_3)_2$), 23.26 (CH(*C*H$_3)_2$), 22.40 (CH(*C*H$_3)_2$), 10.07 (Cp^R-*C*H$_3$), 10.04 (Cp^R-*C*H$_3$), 9.92 (Cp^R-*C*H$_3$), 8.44 (Cp^R-*C*H$_3$). ^{31}P{^{1}H} NMR (202 MHz, DMSO-d_6) (ppm): δ 7.09. ESI-MS (m/z): calcd. for $C_{46}H_{55}ClIrNO_3PS$ 960.2958, found: 960.3144 $[M + H]^+$; ESI-MS (m/z): calcd. for $C_{46}H_{54}ClIrNNaO_3PS$ 982.2777, found: 982.2943 $[M + Na]^+$. Anal. calcd for $C_{46}H_{54}ClIrNO_3PS$: C, 57.57; H, 5.67; N, 1.46. Found: C, 57.23; H, 5.59; N, 1.52.

4.3.4. Ir3.

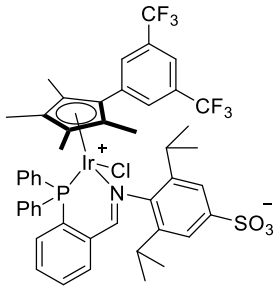

Orange-yellow powder, yield: 174.2 mg (63.7%). ^{1}H NMR (400 MHz, DMSO-d_6) (ppm): δ 8.77 (d, J = 2.3 Hz, 1H, C*H*═N), 8.56 (s, 2H), 8.29 (s, 1H), 8.05 (d, J = 2.1 Hz, 1H), 7.85−7.79 (m, 5H), 7.61 (m, 1H), 7.50−7.40 (m, 6H), 7.29−7.17 (m, 2H), 7.03−6.90 (m, 1H), 3.25−3.17 (m, 1H, C*H*$(CH_3)_2$), 1.99−1.84 (m, 1H, C*H*$(CH_3)_2$), 1.44 (d, J = 1.7 Hz, 3H, Cp^R-C*H*$_3$), 1.35 (s, 3H, Cp^R-C*H*$_3$), 1.27 (s, 3H, Cp^R-C*H*$_3$), 0.96 (d, J = 5.9 Hz, 6H, CH(C*H*$_3)_2$), 0.88 (d, J = 2.3 Hz, 3H, Cp^R-C*H*$_3$), 0.54 (d, J = 6.5 Hz, 3H, CH(C*H*$_3)_2$), 0.26 (d, J = 6.5 Hz, 3H, CH(C*H*$_3)_2$). ^{13}C{^{1}H} NMR (101 MHz, DMSO-d_6) (ppm): δ 176.53 (CH═N), 150.21, 149.00, 140.29, 140.02, 137.66, 137.57, 135.56, 135.45, 135.32, 135.25, 134.15, 134.04, 133.70, 133.63, 133.52, 133.35, 133.25, 131.29, 130.96, 130.62, 130.51, 129.59, 129.48, 128.13, 127.24, 127.03, 126.81, 126.65, 126.47, 125.80, 125.65, 125.18, 124.98, 122.31, 122.26, 121.83, 121.31, 27.51 (*C*H$(CH_3)_2$), 27.12 (*C*H$(CH_3)_2$), 26.05 (CH(*C*H$_3)_2$), 25.55 (CH(*C*H$_3)_2$), 22.63 (CH(*C*H$_3)_2$), 21.45 (CH(*C*H$_3)_2$), 10.12 (Cp^R-*C*H$_3$), 9.98 (Cp^R-*C*H$_3$), 9.35 (Cp^R-*C*H$_3$), 8.84 (Cp^R-*C*H$_3$). ^{31}P{^{1}H} NMR (162 MHz, DMSO-d_6) (ppm): δ 7.11. ESI-MS (m/z): calcd. for $C_{48}H_{47}ClF_6IrNO_3PS$ 1090.2236, found: 1090.2216 $[M + H]^+$; ESI-MS (m/z): calcd. for $C_{48}H_{46}ClF_6IrNNaO_3PS$ 1112.2056, found: 1112.2030 $[M + Na]^+$. Anal. calcd for $C_{48}H_{46}ClF_6IrNO_3PS$: C, 52.91; H, 4.26; N, 1.29. Found: C, 52.68; H, 4.19; N, 1.36.

https://doi.org/10.1021/acs.inorgchem.2c03279
Inorg. Chem. 2022, 61, 20008−20025

4.3.5. Ir4.

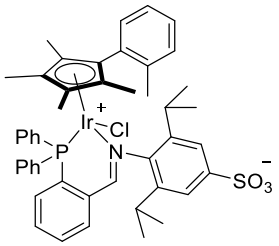

Orange-yellow powder, yield: 149.8 mg (61.7%). ^{1}H NMR (500 MHz, DMSO-d_6) (ppm): δ 8.80 (d, J = 2.5 Hz, 1H, C*H*═N), 8.09−8.07 (m, 1H), 7.85−7.74 (m, 6H), 7.65−7.63 (m, 1H), 7.57 (t, J = 5.7 Hz, 4H), 7.49 (d, J = 1.4 Hz, 1H), 7.41 (d, J = 1.3 Hz, 1H), 7.31−7.21 (m, 4H), 7.19−7.16 (t, 1H), 7.03 (m, 1H), 3.52 (m, 1H, C*H*(CH$_3$)$_2$), 2.08−2.00 (m, 1H, C*H*(CH$_3$)$_2$), 1.90 (s, 3H, aryl-C*H*$_3$), 1.54 (d, 3H, Cp^R-C*H*$_3$), 1.22 (s, 3H, Cp^R-C*H*$_3$), 1.10 (s, 1H, Cp^R-C*H*$_3$), 1.09−1.07 (m, 4H, Cp^R-C*H*$_3$), 1.02 (d, 3H, CH(C*H*$_3$)$_2$), 0.97 (d, 3H, CH(C*H*$_3$)$_2$), 0.95 (s, 1H, Cp^R-C*H*$_3$), 0.65 (d, 3H, CH(C*H*$_3$)$_2$), 0.29 (d, 3H, CH(C*H*$_3$)$_2$). ^{13}C{^{1}H} NMR (126 MHz, DMSO-d_6) (ppm): δ 176.52 (*C*H═N), 150.40, 148.66, 140.70, 139.96, 137.58, 135.56, 135.49, 135.15, 134.51, 134.43, 133.58, 133.49, 133.11, 133.07, 130.37, 129.64, 129.62, 129.59, 129.54, 129.36, 129.33, 128.88, 128.82, 128.80, 127.30, 127.28, 126.84, 126.83, 126.57, 126.33, 126.30, 126.08, 126.06, 125.60, 121.90, 121.17, 27.55 (*C*H(CH$_3$)$_2$), 27.06 (*C*H(CH$_3$)$_2$), 26.03 (CH(*C*H$_3$)$_2$), 25.77 (CH(*C*H$_3$)$_2$), 23.57 (CH(*C*H$_3$)$_2$), 22.67 (CH(*C*H$_3$)$_2$), 19.61 (aryl-*C*H$_3$), 9.86 (Cp^R-*C*H$_3$), 9.60 (Cp^R-*C*H$_3$), 9.21 (Cp^R-*C*H$_3$), 8.78 (Cp^R-*C*H$_3$). ^{31}P{^{1}H} NMR (202 MHz, DMSO-d_6) (ppm): δ 6.21. ESI-MS (m/z): calcd. for $C_{47}H_{51}ClIrNO_3PS$ 968.2645, found: 968.2819 [M + H]$^+$; ESI-MS (m/z): calcd. for $C_{47}H_{50}ClIrNNaO_3PS$ 990.2464, found: 990.2629 [M + Na]$^+$. Anal. calcd for $C_{47}H_{50}ClIrNO_3PS$: C, 58.34; H, 5.21; N, 1.45. Found: C, 58.13; H, 5.29; N, 1.31.

4.3.6. Rh1.

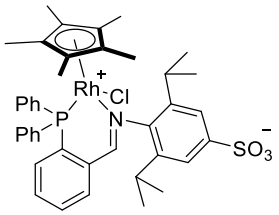

Orange-red powder, yield: 70.4 mg (69.3%). ^{1}H NMR (500 MHz, DMSO-d_6) (ppm): δ 8.61 (s, 1H, C*H*═N), 7.97−7.95 (m, 1H), 7.82−7.71 (m, 7H), 7.71−7.63 (m, 3H), 7.59 (d, J = 1.7 Hz, 1H), 7.40 (d, J = 1.7 Hz, 1H), 7.23−7.19 (m, 2H), 6.99−6.95 (m, 1H), 3.54−3.47 (m, 1H, C*H*(CH$_3$)$_2$), 1.91−1.82 (m, 1H, C*H*(CH$_3$)$_2$), 1.36 (d, J = 6.7 Hz, 3H, CH(C*H*$_3$)$_2$), 1.15 (d, J = 3.8 Hz, 15H, Cp^R-C*H*$_3$), 1.03 (d, J = 6.6 Hz, 3H, CH(C*H*$_3$)$_2$), 0.97 (d, J = 6.6 Hz, 3H, CH(C*H*$_3$)$_2$), 0.16 (d, J = 6.6 Hz, 3H, CH(C*H*$_3$)$_2$). ^{13}C{^{1}H} NMR (151 MHz, DMSO-d_6) (ppm): δ 176.08 (*C*H═N), 149.93, 148.44, 140.66, 139.07, 137.76, 135.66, 134.39, 134.32, 133.59, 133.52, 133.17, 132.92, 130.50, 130.43, 129.75, 129.68, 127.95, 127.65, 127.50, 127.16, 126.46, 126.13, 122.02, 121.08, 103.24, 27.73 (*C*H(CH$_3$)$_2$), 27.02 (*C*H(CH$_3$)$_2$), 25.76 (CH-(*C*H$_3$)$_2$), 25.68 (CH(*C*H$_3$)$_2$), 23.26 (CH(*C*H$_3$)$_2$), 22.26 (CH(*C*H$_3$)$_2$), 9.25 (Cp^R-*C*H$_3$), 9.03 (Cp^R-*C*H$_3$). ^{31}P{^{1}H} NMR (202 MHz, DMSO-d_6) (ppm): δ 37.61, 36.91. ESI-MS (m/z): calcd. for $C_{41}H_{47}ClNO_3PRhS$ 802.1758, found: 802.1865 [M + H]$^+$; ESI-MS (m/z): calcd. for $C_{41}H_{46}ClNNaO_3PRhS$ 824.1577, found: 824.1677 [M + Na]$^+$. Anal. calcd for $C_{41}H_{46}ClNO_3PRhS$: C, 61.39; H, 5.78; N, 1.75. Found: C, 61.68; H, 5.69; N, 1.67.

4.3.7. Rh2.

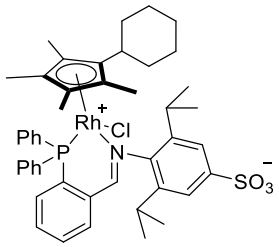

Orange-red powder, yield: 137.8 mg (63.1%). ^{1}H NMR (500 MHz, DMSO-d_6) (ppm): δ 8.58 (s, 1H, C*H*═N), 7.96−7.94 (m, 1H), 7.77 (s, 1H), 7.76−7.73 (m, 5H), 7.72−7.69 (m, 2H), 7.66 (t, J = 6.1 Hz, 2H), 7.60 (s, 1H), 7.42 (s, 1H), 7.28−7.24 (m, 2H), 7.04−7.00 (m, 1H), 3.64−3.55 (m, 1H, C*H*(CH$_3$)$_2$), 2.07 (s, 6H, Cy-C*H*$_2$), 1.96−1.88 (m, 1H, C*H*(CH$_3$)$_2$), 1.83−1.81 (m, 1H, Cy-C*H*$_2$), 1.69−1.66 (m, 1H, Cy-C*H*$_2$), 1.64−1.58 (m, 2H, Cy-C*H*$_2$), 1.39−1.37 (m, 6H, Cp^R-C*H*$_3$), 1.27 (d, J = 3.4 Hz, 3H, Cp^R-C*H*$_3$), 1.24 (d, J = 5.2 Hz, 3H, Cp^R-C*H*$_3$), 1.01 (t, J = 6.8 Hz, 7H, (CH(C*H*$_3$)$_2$, 6H)+(Cy-C*H*, 1H)), 0.91 (d, J = 3.1 Hz, 3H, CH(C*H*$_3$)$_2$), 0.17 (d, J = 6.5 Hz, 3H, CH(C*H*$_3$)$_2$). ^{13}C{^{1}H} NMR (126 MHz, DMSO-d_6) (ppm): δ 176.44 (*C*H═N), 150.10, 149.21, 148.23, 144.23, 140.86, 139.14, 136.51, 135.21, 134.08, 133.92, 130.47, 129.69, 129.40, 129.35, 127.89, 127.47, 126.94, 126.55, 121.97, 121.22, 120.62, 120.07, 111.02, 106.93, 104.93, 103.66, 99.35, 98.61, 97.98, 35.63 (Cy-CH), 30.33 (Cy-*C*H$_2$), 29.99 (Cy-*C*H$_2$), 27.75 (*C*H(CH$_3$)$_2$), 27.36 (*C*H(CH$_3$)$_2$), 26.85 (Cy-*C*H$_2$), 25.99 (Cy-*C*H$_2$), 25.80 (Cy-*C*H$_2$), 25.66 (CH(*C*H$_3$)$_2$), 23.60 (CH(*C*H$_3$)$_2$), 23.37 (CH-(*C*H$_3$)$_2$), 22.25 (CH(*C*H$_3$)$_2$), 10.60 (Cp^R-*C*H$_3$), 10.40 (Cp^R-*C*H$_3$), 10.15 (Cp^R-*C*H$_3$), 9.07 (Cp^R-*C*H$_3$). ^{31}P{^{1}H} NMR (202 MHz, DMSO-d_6) (ppm): δ 37.63, 36.94. ESI-MS (m/z): calcd. for $C_{46}H_{55}ClNO_3PRhS$ 870.2384, found: 870.2367 [M + H]$^+$; ESI-MS (m/z): calcd. for $C_{46}H_{54}ClNNaO_3PRhS$ 892.2203, found: 892.2175 [M + Na]$^+$. Anal. calcd for $C_{46}H_{54}ClNO_3PRhS$: C, 63.48; H, 6.25; N, 1.61. Found: C, 63.75; H, 6.17; N, 1.58.

4.3.8. Rh3.

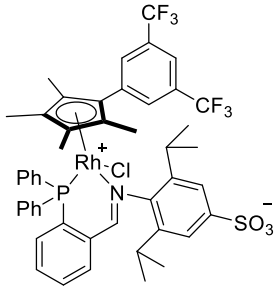

Orange-red powder, yield: 166.7 mg (66.4%). ^{1}H NMR (400 MHz, DMSO-d_6) (ppm): δ 8.69 (s, 1H, C*H*═N), 8.31 (s, 1H), 8.05−7.99 (m, 1H), 7.85−7.68 (m, 7H), 7.61−7.59 (m, 3H), 7.39 (d, J = 2.8 Hz, 3H), 7.26−7.17 (m, 3H), 6.96−6.91 (m, 1H), 3.32−3.26 (m, 1H, C*H*(CH$_3$)$_2$), 2.60−2.55 (m, 1H, C*H*(CH$_3$)$_2$), 1.36 (s, 3H, Cp^R-C*H*$_3$), 1.34 (d, J = 5.7 Hz, 3H, Cp^R-C*H*$_3$), 1.25 (s, 3H, Cp^R-C*H*$_3$), 0.90 (d, J = 6.4 Hz, 6H, CH(C*H*$_3$)$_2$), 0.75 (d, J = 3.3 Hz, 3H, Cp^R-C*H*$_3$), 0.40 (d, J = 6.5 Hz, 3H, CH(C*H*$_3$)$_2$), 0.29 (d, J = 6.4 Hz, 3H, CH(C*H*$_3$)$_2$).

https://doi.org/10.1021/acs.inorgchem.2c03279
Inorg. Chem. 2022, 61, 20008−20025

$^{13}C\{^1H\}$ NMR (101 MHz, DMSO-d_6) (ppm): δ 176.81 (*C*H═N), 149.56, 148.66, 140.47, 139.79, 135.75, 135.63, 135.02, 134.60, 134.50, 133.73, 133.66, 133.55, 133.33, 133.16, 132.00, 131.34, 131.01, 130.81, 130.70, 129.98, 129.88, 129.69, 129.45, 129.39, 127.68, 127.47, 127.01, 126.68, 126.14, 125.63, 125.12, 124.97, 123.46, 122.25, 121.86, 121.37, 121.26, 27.70 (*C*H(CH_3)$_2$), 27.49 (*C*H(CH_3)$_2$), 26.32 (CH(*C*H$_3$)$_2$), 25.50 (CH(*C*H$_3$)$_2$), 22.55 (CH(*C*H$_3$)$_2$), 21.18 (CH(*C*H$_3$)$_2$), 10.47 (Cp^R-*C*H$_3$), 10.16 (Cp^R-*C*H$_3$), 9.76 (Cp^R-*C*H$_3$), 9.21 (Cp^R-*C*H$_3$). $^{31}P\{^1H\}$ NMR (162 MHz, DMSO-d_6) (ppm): δ 40.16, 39.29. ESI-MS (m/z): calcd. for $C_{48}H_{47}ClF_6NO_3PRhS$ 1000.1662, found: 1000.1649 $[M + H]^+$; ESI-MS (m/z): calcd. for $C_{48}H_{46}ClF_6NNaO_3PRhS$ 1022.1481, found: 1022.1463 $[M + Na]^+$. Anal. calcd for $C_{48}H_{46}ClF_6NO_3PRhS$: C, 57.64; H, 4.64; N, 1.40. Found: C, 57.48; H, 4.69; N, 1.33.

4.3.9. Ru1.

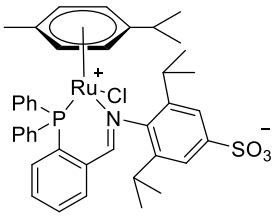

Orange-brown powder, yield: 65.8 mg (65.5%). ^1H NMR (500 MHz, DMSO-d_6) (ppm): δ 8.61 (d, J = 2.4 Hz, 1H, C*H*═N), 8.00−7.97 (m, 1H), 7.94−7.86 (m, 2H), 7.78−7.74 (m, 1H), 7.74−7.63 (m, 7H), 7.61 (t, J = 7.6 Hz, 1H), 7.48−7.38 (m, 3H), 7.02−6.98 (m, 1H), 6.36−6.29 (m, 1H, arene-*H*), 5.71 (d, J = 6.2 Hz, 1H, arene-*H*), 5.11 (d, J = 6.0 Hz, 1H, arene-*H*), 4.65 (d, J = 6.4 Hz, 1H, arene-*H*), 4.04−3.97 (m, 1H, C*H*(CH_3)$_2$), 2.57−2.52 (m, 1H, C*H*(CH_3)$_2$), 1.91−1.83 (m, 1H, C*H*(CH_3)$_2$), 1.49 (d, J = 6.7 Hz, 3H, CH(C*H*$_3$)$_2$), 1.39 (s, 3H, arene-C*H*$_3$), 1.22 (d, J = 7.0 Hz, 3H, CH(C*H*$_3$)$_2$), 1.15 (d, J = 6.9 Hz, 3H, CH(C*H*$_3$)$_2$), 1.05 (d, J = 6.6 Hz, 3H, CH(C*H*$_3$)$_2$), 0.87 (d, J = 6.7 Hz, 3H, CH(C*H*$_3$)$_2$), 0.78 (d, J = 6.5 Hz, 3H, CH(C*H*$_3$)$_2$). $^{13}C\{^1H\}$ NMR (151 MHz, DMSO-d_6) (ppm): δ 176.88 (*C*H═N), 154.99, 148.54, 139.75, 139.25, 137.76, 136.41, 135.63, 135.56, 135.04, 133.41, 133.01, 132.69, 132.58, 132.11, 131.13, 130.81, 129.71, 128.96, 128.59, 125.62, 125.30, 124.94, 122.39, 121.38, 100.41 (arene-*C*), 100.30 (arene-*C*), 91.58 (arene-*C*), 91.52 (arene-*C*), 90.39 (arene-*C*), 78.33 (arene-*C*), 31.31 (*C*H(CH_3)$_2$), 27.58 (*C*H(CH_3)$_2$), 27.40 (*C*H(CH_3)$_2$), 26.80 (CH(*C*H$_3$)$_2$), 26.36 (CH(*C*H$_3$)$_2$), 22.89 (CH(*C*H$_3$)$_2$), 22.57 (CH(*C*H$_3$)$_2$), 21.98 (CH(*C*H$_3$)$_2$), 21.92 (CH(*C*H$_3$)$_2$), 16.48 (arene-*C*H$_3$). $^{31}P\{^1H\}$ NMR (202 MHz, DMSO-d_6) (ppm): δ 39.03. ESI-MS (m/z): calcd. for $C_{41}H_{46}ClNO_3PRuS$ 800.1668, found: 800.1791 $[M + H]^+$; ESI-MS (m/z): calcd. for $C_{41}H_{45}ClNNaO_3PRuS$ 822.1487, found: 822.1604 $[M + Na]^+$. Anal. calcd for $C_{41}H_{45}ClNO_3PRuS$: C, 61.60; H, 5.67; N, 1.75. Found: C, 61.72; H, 5.63; N, 1.70.

4.3.10. Ru2.

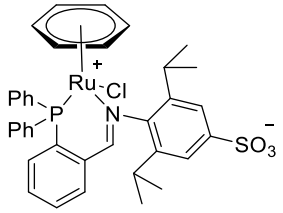

Brown powder, yield: 122.6 mg (65.7%). ^1H NMR (500 MHz, DMSO-d_6) (ppm): δ 8.61 (d, J = 2.1 Hz, 1H, C*H*═N), 7.94−7.92 (m, 1H), 7.81−7.62 (m, 11H), 7.42−7.38 (t, 3H), 6.85−6.81 (m, 1H), 5.62 (s, 6H, arene-*H*), 3.93−3.86 (m, 1H, C*H*(CH_3)$_2$), 1.76−1.68 (m, 1H, C*H*(CH_3)$_2$), 1.46 (d, J = 6.7 Hz, 3H, CH(C*H*$_3$)$_2$), 1.11 (d, J = 6.7 Hz, 3H, CH(C*H*$_3$)$_2$), 0.71 (d, J = 6.7 Hz, 3H, CH(C*H*$_3$)$_2$), 0.60 (d, J = 6.6 Hz, 3H, CH(C*H*$_3$)$_2$). $^{13}C\{^1H\}$ NMR (126 MHz, DMSO-d_6) (ppm): δ 175.29 (*C*H═N), 155.35, 148.62, 139.39, 138.80, 137.39, 136.29, 135.40, 135.03, 133.40, 133.16, 132.82, 132.75, 132.64, 132.23, 130.26, 130.18, 130.04, 129.96, 129.39, 128.96, 124.79, 124.40, 122.29, 120.95, 93.62 (arene-*C*), 27.75 (*C*H(CH_3)$_2$), 27.54 (*C*H(CH_3)$_2$), 26.53 (CH(*C*H$_3$)$_2$), 26.17 (CH(*C*H$_3$)$_2$), 22.64 (CH(*C*H$_3$)$_2$), 21.56 (CH(*C*H$_3$)$_2$). $^{31}P\{^1H\}$ NMR (202 MHz, DMSO-d_6) (ppm): δ 39.40. ESI-MS (m/z): calcd. for $C_{37}H_{38}ClNO_3PRuS$ 744.1042, found: 744.1140 $[M + H]^+$; ESI-MS (m/z): calcd. for $C_{37}H_{37}ClNNaO_3PRuS$ 766.0861, found: 766.0952 $[M + Na]^+$. Anal. calcd for $C_{37}H_{37}ClNO_3PRuS$: C, 59.79; H, 5.02; N, 1.88. Found: C, 59.98; H, 5.08; N, 1.79.

4.3.11. Ru3.

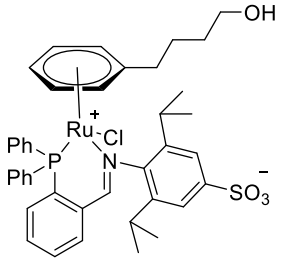

Orange-brown powder, yield: 68.0 mg (66.4%). ^1H NMR (500 MHz, DMSO-d_6) (ppm): δ 8.59 (d, J = 2.3 Hz, 1H, C*H*═N), 7.94−7.91 (m, 1H), 7.82−7.56 (m, 11H), 7.45−7.31 (m, 3H), 6.83−6.79 (m, 1H), 6.22−6.19 (m, 1H, arene-*H*), 5.43 (d, J = 6.0 Hz, 1H, arene-*H*), 5.32 (d, J = 6.1 Hz, 1H, arene-*H*), 5.11 (t, J = 5.5 Hz, 1H, arene-*H*), 4.49 (t, J = 6.0 Hz, 1H, arene-*H*), 4.43 (t, J = 5.2 Hz, 1H, $(CH_2)_4OH$), 3.89−3.77 (m, 1H, C*H*(CH_3)$_2$), 3.41−3.38 (m, 2H, $(CH_2)_4OH$), 2.55−2.53 (m, 1H, C*H*(CH_3)$_2$), 2.39−2.31 (m, 1H, $(CH_2)_4OH$), 1.74−1.69(m, 1H, $(CH_2)_4OH$), 1.67−1.57 (m, 2H, $(CH_2)_4OH$), 1.46 (d, J = 6.7 Hz, 3H, CH(C*H*$_3$)$_2$), 1.45−1.36 (m, 2H, $(CH_2)_4OH$), 1.08 (d, J = 6.6 Hz, 3H, CH(C*H*$_3$)$_2$), 0.67 (d, J = 6.8 Hz, 3H, CH(C*H*$_3$)$_2$), 0.59 (d, J = 6.6 Hz, 3H, CH(C*H*$_3$)$_2$). $^{13}C\{^1H\}$ NMR (101 MHz, DMSO-d_6) (ppm): δ 175.42 (*C*H═N), 154.85, 148.83, 139.16, 139.01, 137.27, 136.49, 135.33, 135.23, 133.71, 133.11, 132.80, 132.56, 132.20, 130.31, 130.21, 130.08, 129.97, 129.66, 129.12, 125.20, 124.71, 122.23, 122.12, 121.08, 99.86 (arene-*C*), 95.99 (arene-*C*), 95.89 (arene-*C*), 91.23 (arene-*C*), 83.34 (arene-*C*), 82.14 (arene-*C*), 60.74 ($(CH_2)_4OH$), 33.39 ($(CH_2)_4OH$), 32.53 ($(CH_2)_4OH$), 27.68 ($(CH_2)_4OH$), 27.59 (*C*H(CH_3)$_2$), 26.46 (*C*H(CH_3)$_2$), 26.25 (CH(*C*H$_3$)$_2$), 25.96 (CH(*C*H$_3$)$_2$), 22.80 (CH(*C*H$_3$)$_2$), 21.76 (CH(*C*H$_3$)$_2$). $^{31}P\{^1H\}$ NMR (202 MHz, DMSO-d_6) (ppm): δ 39.21. ESI-MS (m/z): calcd. for $C_{41}H_{46}ClNO_4PRuS$ 816.1617, found: 816.1742 $[M + H]^+$; ESI-MS (m/z): calcd. for $C_{41}H_{45}ClNNaO_4PRuS$ 838.1437, found: 838.1549 $[M + Na]^+$. Anal. calcd for $C_{41}H_{45}ClNO_4PRuS$: C, 60.40; H, 5.56; N, 1.72. Found: C, 60.11; H, 5.63; N, 1.82.

https://doi.org/10.1021/acs.inorgchem.2c03279
Inorg. Chem. 2022, 61, 20008−20025

■ ASSOCIATED CONTENT

Supporting Information

The Supporting Information is available free of charge at https://pubs.acs.org/doi/10.1021/acs.inorgchem.2c03279.

Additional experimental details and methods, ^{1}H, $^{13}C\{^{1}H\}$, and $^{31}P\{^{1}H\}$ NMR spectra, and ESI-MS spectra for all compounds (Figures S1−S60 and Tables S1−S9) (PDF)

Accession Codes

CCDC 2205155, 2205157, and 2216236 contain the supplementary crystallographic data for this paper. These data can be obtained free of charge via www.ccdc.cam.ac.uk/data_request/cif, or by emailing data_request@ccdc.cam.ac.uk, or by contacting The Cambridge Crystallographic Data Centre, 12 Union Road, Cambridge CB2 1EZ, UK; fax: +44 1223 336033.

■ AUTHOR INFORMATION

Corresponding Authors

Lihua Guo − *School of Chemistry and Chemical Engineering, Qufu Normal University, Qufu 273165, P. R. China;* orcid.org/0000-0002-0842-9958; Email: guolihua@qfnu.edu.cn

Zhe Liu − *School of Chemistry and Chemical Engineering, Qufu Normal University, Qufu 273165, P. R. China;* orcid.org/0000-0001-5796-4335; Email: liuzheqd@163.com

Authors

Xueyan Hu − *School of Chemistry and Chemical Engineering, Qufu Normal University, Qufu 273165, P. R. China*

Mengqi Liu − *School of Chemistry and Chemical Engineering, Qufu Normal University, Qufu 273165, P. R. China*

Qiuya Zhang − *School of Chemistry and Chemical Engineering, Qufu Normal University, Qufu 273165, P. R. China*

Yuwen Gong − *School of Chemistry and Chemical Engineering, Qufu Normal University, Qufu 273165, P. R. China*

Mengru Sun − *School of Chemistry and Chemical Engineering, Qufu Normal University, Qufu 273165, P. R. China*

Shenghan Feng − *School of Chemistry and Chemical Engineering, Qufu Normal University, Qufu 273165, P. R. China*

Youzhi Xu − *School of Chemistry and Chemical Engineering, Qufu Normal University, Qufu 273165, P. R. China*

Yiming Liu − *School of Chemistry and Chemical Engineering, Qufu Normal University, Qufu 273165, P. R. China*

Complete contact information is available at: https://pubs.acs.org/10.1021/acs.inorgchem.2c03279

Notes

The authors declare no competing financial interest.

■ ACKNOWLEDGMENTS

The authors thank the Natural Science Foundation of Shandong Province (ZR2022MB038), the Young Talents Invitation Program of Shandong Provincial Colleges and Universities, the Taishan Scholars Program, the Youth Tutor Visiting Program of Shandong Province, and the Student's Platform for Innovation and Entrepreneurship Training Program (S202110446047 and XJ20210056) for support.

■ REFERENCES

(1) Cao, Y.; Giovannucci, E. L. Alcohol as a Risk Factor for Cancer. *Semin. Oncol. Nurs.* **2016**, *32*, 325−331.

(2) Tsai, H.-J.; Chang, J. S. Environmental Risk Factors of Pancreatic Cancer. *J. Clin. Med.* **2019**, *8*, 1427.

(3) Dyson, P. J.; Sava, G. Metal-based antitumour drugs in the post genomic era. *Dalton Trans.* **2006**, 1929−1933.

(4) Torigoe, T.; Izumi, H.; Ishiguchi, H.; Yoshida, Y.; Tanabe, M.; Yoshida, T.; Igarashi, T.; Niina, I.; Wakasugi, T.; Imaizumi, T.; Momii, Y.; Kuwano, M.; Kohno, K. Cisplatin Resistance and Transcription Factors. *Curr. Med. Chem.: Anti-Cancer Agents* **2005**, *5*, 15−27.

(5) Matei, D.; Fang, F.; Shen, C.; Schilder, J.; Arnold, A.; Zeng, Y.; Berry, W. A.; Huang, T.; Nephew, K. P. Epigenetic Resensitization to Platinum in Ovarian Cancer. *Cancer Res.* **2012**, *72*, 2197−2205.

(6) Florea, A.-M.; Büsselberg, D. Cisplatin as an Anti-Tumor Drug: Cellular Mechanisms of Activity, Drug Resistance and Induced Side Effects. *Cancers* **2011**, *3*, 1351−1371.

(7) Allardyce, C. S.; Dyson, P. J. Metal-based drugs that break the rules. *Dalton Trans.* **2016**, *45*, 3201−3209.

(8) Oun, R.; Moussa, Y. E.; Wheate, N. J. The side effects of platinum-based chemotherapy drugs: a review for chemists. *Dalton Trans.* **2018**, *47*, 6645−6653.

(9) Zeng, L.; Gupta, P.; Chen, Y.; Wang, E.; Ji, L.; Chao, H.; Chen, Z.-S. The development of anticancer ruthenium(II) complexes: from single molecule compounds to nanomaterials. *Chem. Soc. Rev.* **2017**, *46*, 5771−5804.

(10) Zhang, P.; Sadler, P. J. Redox-Active Metal Complexes for Anticancer Therapy. *Eur. J. Inorg. Chem.* **2017**, *2017*, 1541−1548.

(11) Truong, D.; Sullivan, M. P.; Tong, K. K. H.; Steel, T. R.; Prause, A.; Lovett, J. H.; Andersen, J. W.; Jamieson, S. M. F.; Harris, H. H.; Ott, I.; Weekley, C. M.; Hummitzsch, K.; Söhnel, T.; Hanif, M.; Metzler-Nolte, N.; Goldstone, D. C.; Hartinger, C. G. Potent Inhibition of Thioredoxin Reductase by the Rh Derivatives of Anticancer M(arene/Cp*)(NHC)Cl_2 Complexes. *Inorg. Chem.* **2020**, *59*, 3281−3289.

(12) Pérez-Arnaiz, C.; Acuña, M. I.; Busto, N.; Echevarría, I.; Martínez-Alonso, M.; Espino, G.; García, B.; Domínguez, F. Thiabendazole-based Rh(III) and Ir(III) biscyclometallated complexes with mitochondria-targeted anticancer activity and metal-sensitive photodynamic activity. *Eur. J. Med. Chem.* **2018**, *157*, 279−293.

(13) Rubio, A. R.; González, R.; Busto, N.; Vaquero, M.; Iglesias, A. L.; Jalón, F. A.; Espino, G.; Rodríguez, A. M.; García, B.; Manzano, B. R. Anticancer Activity of Half-Sandwich Ru, Rh and Ir Complexes with Chrysin Derived Ligands: Strong Effect of the Side Chain in the Ligand and Influence of the Metal. *Pharmaceutics* **2021**, *13*, 1540.

(14) Konkankit, C. C.; Marker, S. C.; Knopf, K. M.; Wilson, J. J. Anticancer activity of complexes of the third row transition metals, rhenium, osmium, and iridium. *Dalton Trans.* **2018**, *47*, 9934−9974.

(15) Lord, R. M.; Zegke, M.; Basri, A. M.; Pask, C. M.; McGowan, P. C. Rhodium(III) Dihalido Complexes: The Effect of Ligand Substitution and Halido Coordination on Increasing Cancer Cell Potency. *Inorg. Chem.* **2021**, *60*, 2076−2086.

(16) Biancalana, L.; Kostrhunova, H.; Batchelor, L. K.; Hadiji, M.; Degano, I.; Pampaloni, G.; Zacchini, S.; Dyson, P. J.; Brabec, V.; Marchetti, F. Hetero-Bis-Conjugation of Bioactive Molecules to Half-Sandwich Ruthenium(II) and Iridium(III) Complexes Provides Synergic Effects in Cancer Cell Cytotoxicity. *Inorg. Chem.* **2021**, *60*, 9529−9541.

(17) Łomzik, M.; Hanif, M.; Budniok, A.; Błauż, A.; Makal, A.; Tchoń, D. M.; Leśniewska, B.; Tong, K. K. H.; Movassaghi, S.; Söhnel, T.; Jamieson, S. M. F.; Zafar, A.; Reynisson, J.; Rychlik, B.; Hartinger, C. G.; Plażuk, D. Metal-Dependent Cytotoxic and Kinesin Spindle Protein Inhibitory Activity of Ru, Os, Rh, and Ir Half-Sandwich Complexes of Ispinesib-Derived Ligands. *Inorg. Chem.* **2020**, *59*, 14879−14890.

(18) Navale, G.; Singh, S.; Agrawal, S.; Ghosh, C.; Roy Choudhury, A.; Roy, P.; Sarkar, D.; Ghosh, K. DNA binding, antitubercular,

antibacterial and anticancer studies of newly designed piano-stool ruthenium(ii) complexes. *Dalton Trans.* **2022**, *51*, 16371−16382.
(19) Lee, B. Y. T.; Sullivan, M. P.; Yano, E.; Tong, K. K. H.; Hanif, M.; Kawakubo-Yasukochi, T.; Jamieson, S. M. F.; Soehnel, T.; Goldstone, D. C.; Hartinger, C. G. Anthracenyl Functionalization of Half-Sandwich Carbene Complexes: In Vitro Anticancer Activity and Reactions with Biomolecules. *Inorg. Chem.* **2021**, *60*, 14636−14644.
(20) Ramos, R.; Gilles, J.-F.; Morichon, R.; Przybylski, C.; Caron, B.; Botuha, C.; Karaiskou, A.; Salmain, M.; Sobczak-Thépot, J. Cytotoxic BODIPY-Appended Half-Sandwich Iridium(III) Complex Forms Protein Adducts and Induces ER Stress. *J. Med. Chem.* **2021**, *64*, 16675−16686.
(21) Rademaker-Lakhai, J. M.; van den Bongard, D.; Pluim, D.; Beijnen, J. H.; Schellens, J. H. M. A Phase I and Pharmacological Study with Imidazolium-trans-DMSO-imidazole-tetrachlororuthenate, a Novel Ruthenium Anticancer Agent. *Clin. Cancer Res.* **2004**, *10*, 3717−3727.
(22) Hartinger, C. G.; Jakupec, M. A.; Zorbas-Seifried, S.; Groessl, M.; Egger, A.; Berger, W.; Zorbas, H.; Dyson, P. J.; Keppler, B. K. KP1019, A New Redox-Active Anticancer Agent − Preclinical Development and Results of a Clinical Phase I Study in Tumor Patients. *Chem. Biodiversity* **2008**, *5*, 2140−2155.
(23) Lo, K. K.-W. Luminescent Rhenium(I) and Iridium(III) Polypyridine Complexes as Biological Probes, Imaging Reagents, and Photocytotoxic Agents. *Acc. Chem. Res.* **2015**, *48*, 2985−2995.
(24) Bonnet, S. Why develop photoactivated chemotherapy? *Dalton Trans.* **2018**, *47*, 10330−10343.
(25) Tong, K. K. H.; Riisom, M.; Leung, E.; Hanif, M.; Söhnel, T.; Jamieson, S. M. F.; Hartinger, C. G. Impact of Coordination Mode and Ferrocene Functionalization on the Anticancer Activity of N-Heterocyclic Carbene Half-Sandwich Complexes. *Inorg. Chem.* **2022**, *61*, 17226−17241.
(26) Maji, M.; Acharya, S.; Bhattacharya, I.; Gupta, A.; Mukherjee, A. Effect of an Imidazole-Containing Schiff Base of an Aromatic Sulfonamide on the Cytotoxic Efficacy of N,N-Coordinated Half-Sandwich Ruthenium(II) p-Cymene Complexes. *Inorg. Chem.* **2021**, *60*, 4744−4754.
(27) Arunachalam, A.; Rengan, R.; Umapathy, D.; Arockiam, A. J. V. Impact of Biphenyl Benzhydrazone-Incorporated Arene Ru(II) Complexes on Cytotoxicity and the Cancer Cell Death Mechanism. *Organometallics* **2022**, *41*, 2474−2486.
(28) Carrasco, A. C.; Rodríguez-Fanjul, V.; Habtemariam, A.; Pizarro, A. M. Structurally Strained Half-Sandwich Iridium(III) Complexes As Highly Potent Anticancer Agents. *J. Med. Chem.* **2020**, *63*, 4005−4021.
(29) Hearn, J. M.; Romero-Canelón, I.; Qamar, B.; Liu, Z.; Hands-Portman, I.; Sadler, P. J. Organometallic Iridium(III) Anticancer Complexes with New Mechanisms of Action: NCI-60 Screening, Mitochondrial Targeting, and Apoptosis. *ACS Chem. Biol.* **2013**, *8*, 1335−1343.
(30) Liu, Z.; Sadler, P. J. Organoiridium Complexes: Anticancer Agents and Catalysts. *Acc. Chem. Res.* **2014**, *47*, 1174−1185.
(31) Liu, L.-J.; Wang, W.; Huang, S.-Y.; Hong, Y.; Li, G.; Lin, S.; Tian, J.; Cai, Z.; Wang, H.-M. D.; Ma, D.-L.; Leung, C.-H. Inhibition of the Ras/Raf interaction and repression of renal cancer xenografts in vivo by an enantiomeric iridium(III) metal-based compound. *Chem. Sci.* **2017**, *8*, 4756−4763.
(32) Kang, T.-S.; Wang, W.; Zhong, H.-J.; Dong, Z.-Z.; Huang, Q.; Mok, S. W. F.; Leung, C.-H.; Wong, V. K. W.; Ma, D.-L. An anti-prostate cancer benzofuran-conjugated iridium(III) complex as a dual inhibitor of STAT3 and NF-κB. *Cancer Lett.* **2017**, *396*, 76−84.
(33) Liu, Z.; Habtemariam, A.; Pizarro, A. M.; Fletcher, S. A.; Kisova, A.; Vrana, O.; Salassa, L.; Bruijnincx, P. C. A.; Clarkson, G. J.; Brabec, V.; Sadler, P. J. Organometallic Half-Sandwich Iridium Anticancer Complexes. *J. Med. Chem.* **2011**, *54*, 3011−3026.
(34) Balaji, S.; Mohamed Subarkhan, M. K.; Ramesh, R.; Wang, H.; Semeril, D. Synthesis and Structure of Arene Ru(II) N^O-Chelating Complexes: In Vitro Cytotoxicity and Cancer Cell Death Mechanism. *Organometallics* **2020**, *39*, 1366−1375.
(35) Liu, Z.; Salassa, L.; Habtemariam, A.; Pizarro, A. M.; Clarkson, G. J.; Sadler, P. J. Contrasting Reactivity and Cancer Cell Cytotoxicity of Isoelectronic Organometallic Iridium(III) Complexes. *Inorg. Chem.* **2011**, *50*, 5777−5783.
(36) Liu, Z.; Habtemariam, A.; Pizarro, A. M.; Clarkson, G. J.; Sadler, P. J. Organometallic Iridium(III) Cyclopentadienyl Anticancer Complexes Containing C,N-Chelating Ligands. *Organometallics* **2011**, *30*, 4702−4710.
(37) Liu, Z.; Romero-Canelón, I.; Habtemariam, A.; Clarkson, G. J.; Sadler, P. J. Potent Half-Sandwich Iridium(III) Anticancer Complexes Containing C^N-Chelated and Pyridine Ligands. *Organometallics* **2014**, *33*, 5324−5333.
(38) Liu, Z.; Romero-Canelón, I.; Qamar, B.; Hearn, J. M.; Habtemariam, A.; Barry, N. P. E.; Pizarro, A. M.; Clarkson, G. J.; Sadler, P. J. The Potent Oxidant Anticancer Activity of Organoiridium Catalysts. *Angew. Chem., Int. Ed.* **2014**, *53*, 3941−3946.
(39) Zhang, H.; Guo, L.; Tian, Z.; Tian, M.; Zhang, S.; Xu, Z.; Gong, P.; Zheng, X.; Zhao, J.; Liu, Z. Significant effects of counteranions on the anticancer activity of iridium(iii) complexes. *Chem. Commun.* **2018**, *54*, 4421−4424.
(40) Yang, Y.; Ge, X.; Guo, L.; Zhu, T.; Tian, Z.; Zhang, H.; Du, Q.; Peng, H.; Ma, W.; Liu, Z. Zwitterionic and cationic half-sandwich iridium(III) ruthenium(II) complexes bearing sulfonate groups: synthesis, characterization and their different biological activities. *Dalton Trans.* **2019**, *48*, 3193−3197.
(41) Yang, Y.; Guo, L.; Ge, X.; Zhu, T.; Chen, W.; Zhou, H.; Zhao, L.; Liu, Z. The Fluorine Effect in Zwitterionic Half-Sandwich Iridium(III) Anticancer Complexes. *Inorg. Chem.* **2020**, *59*, 748−758.
(42) Yang, Y.; Guo, L.; Tian, Z.; Ge, X.; Gong, Y.; Zheng, H.; Shi, S.; Liu, Z. Lysosome-Targeted Phosphine-Imine Half-Sandwich Iridium-(III) Anticancer Complexes: Synthesis, Characterization, and Biological Activity. *Organometallics* **2019**, *38*, 1761−1769.
(43) Reddy, T. S.; Privér, S. H.; Mirzadeh, N.; Bhargava, S. K. Anticancer gold(I) phosphine complexes: Cyclic trimers and tetramers containing the P-Au-P moiety. *J. Inorg. Biochem.* **2017**, *175*, 1−8.
(44) Gorbachuk, E.; Badeeva, E.; Gubaidullin, A.; Samigullina, A.; Voloshina, A.; Sapunova, A.; Hey-Hawkins, E.; Sinyashin, O.; Yakhvarov, D. Bis(α-hydroxycycloalkyl)phosphine Oxides Obtained from White Phosphorus via Phosphine Oxide H_3PO: Synthesis, Molecular Structure, Coordination Properties and Biological Activity. *ChemPlusChem* **2020**, *85*, 958−962.
(45) Velozo-Sá, V. S.; Pereira, L. R.; Lima, A. P.; Mello-Andrade, F.; Rezende, M. R. M.; Goveia, R. M.; Pires, W. C.; Silva, M. M.; Oliveira, K. M.; Ferreira, A. G.; Ellena, J.; Deflon, V. M.; Grisolia, C. K.; Batista, A. A.; Silveira-Lacerda, E. P. In vitro cytotoxicity and in vivo zebrafish toxicity evaluation of Ru(II)/2-mercaptopyrimidine complexes. *Dalton Trans.* **2019**, *48*, 6026−6039.
(46) Murray, B. S.; Babak, M. V.; Hartinger, C. G.; Dyson, P. J. The development of RAPTA compounds for the treatment of tumors. *Coord. Chem. Rev.* **2016**, *306*, 86−114.
(47) Ang, W. H.; Casini, A.; Sava, G.; Dyson, P. J. Organometallic ruthenium-based antitumor compounds with novel modes of action. *J. Organomet. Chem.* **2011**, *696*, 989−998.
(48) Hartinger, C. G.; Dyson, P. J. Bioorganometallic chemistry—from teaching paradigms to medicinal applications. *Chem. Soc. Rev.* **2009**, *38*, 391−401.
(49) Keter, F. K.; Guzei, I. A.; Nell, M.; Zyl, W. E.; Darkwa, J. Phosphinogold(I) Dithiocarbamate Complexes: Effect of the Nature of Phosphine Ligand on Anticancer Properties. *Inorg. Chem.* **2014**, *53*, 2058−2067.
(50) Mirabell, C. K.; Johnson, R. K.; Hill, D. T.; Faucette, L. F.; Girard, G. R.; Kuo, G. Y.; Sung, C. M.; Crooke, S. T. Correlation of the in vitro cytotoxic and in vivo antitumor activities of gold(I) coordination complexes. *J. Med. Chem.* **1986**, *29*, 218−223.
(51) Gandin, V.; Fernandes, A. P.; Rigobello, M. P.; Dani, B.; Sorrentino, F.; Tisato, F.; Björnstedt, M.; Bindoli, A.; Sturaro, A.; Rella, R.; Marzano, C. Cancer cell death induced by phosphine gold(I) compounds targeting thioredoxin reductase. *Biochem. Pharmacol.* **2010**, *79*, 90−101.

https://doi.org/10.1021/acs.inorgchem.2c03279
Inorg. Chem. 2022, 61, 20008−20025

(52) Du, Q.; Guo, L.; Ge, X.; Zhao, L.; Tian, Z.; Liu, X.; Zhang, F.; Liu, Z. Serendipitous Synthesis of Five-Coordinated Half-Sandwich Aminoimine Iridium(III) and Ruthenium(II) Complexes and Their Application as Potent Anticancer Agents. *Inorg. Chem.* **2019**, *58*, 5956−5965.
(53) Yang, Y.; Guo, L.; Huang, J.; Ji, M.; Ge, X.; Chen, W.; Zhou, H.; Li, X.; Tuo, S.; Liu, Z. Fortuitous synthesis of unsaturated half-sandwich Ruthenium(II) complexes via solvent-involved rearrangement and their biological evaluation. *Dyes Pigm.* **2021**, *184*, No. 108867.
(54) Reiner, T.; Waibel, M.; Marziale, A. N.; Jantke, D.; Kiefer, F. J.; Fässler, T. F.; Eppinger, J. η^6-Arene complexes of ruthenium and osmium with pendant donor functionalities. *J. Organomet. Chem.* **2010**, *695*, 2667−2672.
(55) Tönnemann, J.; Risse, J.; Grote, Z.; Scopelliti, R.; Severin, K. Efficient and Rapid Synthesis of Chlorido-Bridged Half-Sandwich Complexes of Ruthenium, Rhodium, and Iridium by Microwave Heating. *Eur. J. Inorg. Chem.* **2013**, *2013*, 4558−4562.
(56) Sunesh, C. D.; Mathai, G.; Cho, Y.-R.; Choe, Y. Optoelectronic properties of green and yellow light-emitting electrochemical cells based on cationic iridium complexes. *Polyhedron* **2013**, *57*, 77−82.
(57) Gao, J.; Guo, L.; Wu, Y.; Cheng, Y.; Hu, X.; Liu, J.; Liu, Z. 16-Electron Half-Sandwich Rhodium(III), Iridium(III), and Ruthenium-(II) Complexes as Lysosome-Targeted Anticancer Agents. *Organometallics* **2021**, *40*, 3999−4010.
(58) Brown, L. C.; Ressegue, E.; Merola, J. S. Rapid Access to Derivatized, Dimeric, Ring-Substituted Dichloro(cyclopentadienyl)-rhodium(III) and Iridium(III) Complexes. *Organometallics* **2016**, *35*, 4014−4022.
(59) Rafols, L.; Josa, D.; Aguilà, D.; Barrios, L. A.; Roubeau, O.; Cirera, J.; Soto-Cerrato, V.; Pérez-Tomás, R.; Martínez, M.; Grabulosa, A.; Gamez, P. Piano-Stool Ruthenium(II) Complexes with Delayed Cytotoxic Activity: Origin of the Lag Time. *Inorg. Chem.* **2021**, *60*, 7974−7990.
(60) Swaminathan, S.; Haribabu, J.; Balakrishnan, N.; Vasanthakumar, P.; Karvembu, R. Piano stool Ru(II)-arene complexes having three monodentate legs: A comprehensive review on their development as anticancer therapeutics over the past decade. *Coord. Chem. Rev.* **2022**, *459*, No. 214403.
(61) Guerriero, A.; Oberhauser, W.; Riedel, T.; Peruzzini, M.; Dyson, P. J.; Gonsalvi, L. New Class of Half-Sandwich Ruthenium(II) Arene Complexes Bearing the Water-Soluble CAP Ligand as an in Vitro Anticancer Agent. *Inorg. Chem.* **2017**, *56*, 5514−5518.
(62) Maikoo, S.; Makayane, D.; Booysen, I. N.; Ngubane, P.; Khathi, A. Ruthenium compounds as potential therapeutic agents for type 2 diabetes mellitus. *Eur. J. Med. Chem.* **2021**, *213*, No. 113064.
(63) Levina, A.; Mitra, A.; Lay, P. A. Recent developments in ruthenium anticancer drugs. *Metallomics* **2009**, *1*, 458−470.
(64) Peacock, A. F. A.; Sadler, P. J. Medicinal Organometallic Chemistry: Designing Metal Arene Complexes as Anticancer Agents. *Chem. − Asian J.* **2008**, *3*, 1890−1899.
(65) Reisner, E.; Arion, V. B.; Keppler, B. K.; Pombeiro, A. J. L. Electron-transfer activated metal-based anticancer drugs. *Inorg. Chim. Acta* **2008**, *361*, 1569−1583.
(66) Hohmann, H.; Hellquist, B.; Van Eldik, R. Kinetics and mechanism of the complex formation reactions of diaqua-(ethylenediamine)- and diaqua(tetraethylethylenediamine)palladium-(II) with the purine nucleosides adenosine and inosine. *Inorg. Chem.* **1992**, *31*, 345−351.
(67) Guo, L.; Hu, X.; Yang, Y.; An, W.; Gao, J.; Liu, Q.; Liu, Z. Synthesis and biological evaluation of zwitterionic half-sandwich Rhodium(III) and Ruthenium(II) organometallic complexes. *Bioorg. Chem.* **2021**, *116*, No. 105311.
(68) Zhang, C. X.; Lippard, S. J. New metal complexes as potential therapeutics. *Curr. Opin. Chem. Biol.* **2003**, *7*, 481−489.
(69) Koumousi, E. S.; Zampakou, M.; Raptopoulou, C. P.; Psycharis, V.; Beavers, C. M.; Teat, S. J.; Psomas, G.; Stamatatos, T. C. First Palladium(II) and Platinum(II) Complexes from Employment of 2,6-Diacetylpyridine Dioxime: Synthesis, Structural and Spectroscopic Characterization, and Biological Evaluation. *Inorg. Chem.* **2012**, *51*, 7699−7710.
(70) Petrović, A.; Milutinović, M. M.; Petri, E. T.; Živanović, M.; Milivojević, N.; Puchta, R.; Scheurer, A.; Korzekwa, J.; Klisurić, O. R.; Bogojeski, J. Synthesis of Camphor-Derived Bis(pyrazolylpyridine) Rhodium(III) Complexes: Structure−Reactivity Relationships and Biological Activity. *Inorg. Chem.* **2019**, *58*, 307−319.
(71) Li, J.; Guo, L.; Tian, Z.; Tian, M.; Zhang, S.; Xu, K.; Qian, Y.; Liu, Z. Novel half-sandwich iridium(III) imino-pyridyl complexes showing remarkable in vitro anticancer activity. *Dalton Trans.* **2017**, *46*, 15520−15534.
(72) Mukhopadhyay, S.; Gupta, R. K.; Paitandi, R. P.; Rana, N. K.; Sharma, G.; Koch, B.; Rana, L. K.; Hundal, M. S.; Pandey, D. S. Synthesis, Structure, DNA/Protein Binding, and Anticancer Activity of Some Half-Sandwich Cyclometalated Rh(III) and Ir(III) Complexes. *Organometallics* **2015**, *34*, 4491−4506.
(73) Kang, J.; Liu, Y.; Xie, M.-X.; Li, S.; Jiang, M.; Wang, Y.-D. Interactions of human serum albumin with chlorogenic acid and ferulic acid. *Biochim. Biophys. Acta* **2004**, *1674*, 205−214.
(74) Abou-Zied, O. K.; Al-Shihi, O. I. K. Characterization of Subdomain IIA Binding Site of Human Serum Albumin in its Native, Unfolded, and Refolded States Using Small Molecular Probes. *J. Am. Chem. Soc.* **2008**, *130*, 10793−10801.
(75) Ruiz, J.; Vicente, C.; de Haro, C.; Bautista, D. Novel Bis-C,N-Cyclometalated Iridium(III) Thiosemicarbazide Antitumor Complexes: Interactions with Human Serum Albumin and DNA, and Inhibition of Cathepsin B. *Inorg. Chem.* **2013**, *52*, 974−982.
(76) Yang, Y.; Guo, L.; Tian, Z.; Gong, Y.; Zheng, H.; Zhang, S.; Xu, Z.; Ge, X.; Liu, Z. Novel and Versatile Imine-N-Heterocyclic Carbene Half-Sandwich Iridium(III) Complexes as Lysosome-Targeted Anticancer Agents. *Inorg. Chem.* **2018**, *57*, 11087−11098.
(77) Samari, F.; Hemmateenejad, B.; Shamsipur, M.; Rashidi, M.; Samouei, H. Affinity of Two Novel Five-Coordinated Anticancer Pt(II) Complexes to Human and Bovine Serum Albumins: A Spectroscopic Approach. *Inorg. Chem.* **2012**, *51*, 3454−3464.
(78) He, W.; Li, Y.; Xue, C.; Hu, Z.; Chen, X.; Sheng, F. Effect of Chinese medicine alpinetin on the structure of human serum albumin. *Bioorg. Med. Chem.* **2005**, *13*, 1837−1845.
(79) Wang, F.; Huang, W.; Dai, Z. Spectroscopic investigation of the interaction between riboflavin and bovine serum albumin. *J. Mol. Struct.* **2008**, *875*, 509−514.
(80) Pacheco, M. E.; Bruzzone, L. Synchronous fluorescence spectrometry: Conformational investigation or inner filter effect? *J. Lumin.* **2013**, *137*, 138−142.
(81) Castiñeiras, A.; Fernández-Hermida, N.; García-Santos, I.; Gómez-Rodríguez, L. Neutral Ni^{II}, Pd^{II} and Pt^{II} ONS-pincer complexes of 5-acetylbarbituric-4N-dimethylthiosemicarbazone: synthesis, characterization and properties. *Dalton Trans.* **2012**, *41*, 13486−13495.
(82) Cheng, Z. Studies on the interaction between scopoletin and two serum albumins by spectroscopic methods. *J. Lumin.* **2012**, *132*, 2719−2729.
(83) Li, C.; Yu, M.; Sun, Y.; Wu, Y.; Huang, C.; Li, F. A Nonemissive Iridium(III) Complex That Specifically Lights-Up the Nuclei of Living Cells. *J. Am. Chem. Soc.* **2011**, *133*, 11231−11239.
(84) Sun, B.; Liu, J.; Gao, Y.; Zheng, H.-b.; Li, L.; Hu, Q.-w.; Yuan, H.-q.; Lou, H.-x. Design, synthesis and biological evaluation of nitrogen-containing macrocyclic bisbibenzyl derivatives as potent anticancer agents by targeting the lysosome. *Eur. J. Med. Chem.* **2017**, *136*, 603−618.
(85) Qiu, K.; Chen, Y.; Rees, T. W.; Ji, L.; Chao, H. Organelle-targeting metal complexes: From molecular design to bio-applications. *Coord. Chem. Rev.* **2019**, *378*, 66−86.
(86) Tejedor-Estrada, R.; Nonell, S.; Teixido, J.; Sagrista, M. L.; Mora, M.; Villanueva, A.; Canete, M.; Stockert, J. C. An Artificial Neural Network Model for Predicting the Subcellular Localization of Photosensitisers for Photodynamic Therapy of Solid Tumours. *Curr. Med. Chem.* **2012**, *19*, 2472−2482.

https://doi.org/10.1021/acs.inorgchem.2c03279
Inorg. Chem. 2022, 61, 20008−20025

(87) Horobin, R. W.; Rashid-Doubell, F.; Pediani, J. D.; Milligan, G. Predicting small molecule fluorescent probe localization in living cells using QSAR modeling. 1. Overview and models for probes of structure, properties and function in single cells. *Biotech. Histochem.* **2013**, *88*, 440−460.
(88) Xu, W.; Zeng, Z.; Jiang, J.-H.; Chang, Y.-T.; Yuan, L. Discerning the Chemistry in Individual Organelles with Small-Molecule Fluorescent Probes. *Angew. Chem., Int. Ed.* **2016**, *55*, 13658−13699.
(89) Chen, W.-H.; Luo, G.-F.; Zhang, X.-Z. Recent Advances in Subcellular Targeted Cancer Therapy Based on Functional Materials. *Adv. Mater.* **2019**, *31*, No. 1802725.
(90) Horobin, R. W.; Rashid-Doubell, F. Predicting small molecule fluorescent probe localization in living cells using QSAR modeling. 2. Specifying probe, protocol and cell factors; selecting QSAR models; predicting entry and localization. *Biotech. Histochem.* **2013**, *88*, 461−476.
(91) Boya, P.; Kroemer, G. Lysosomal membrane permeabilization in cell death. *Oncogene* **2008**, *27*, 6434−6451.
(92) Britovsek, G. J. P.; Woo, G. Y. Y.; Assavathorn, N. Synthesis and reactivity of water-soluble platinum(II) complexes containing nitrogen ligands. *J. Organomet. Chem.* **2003**, *679*, 110−115.
(93) Allardyce, C. S.; Dyson, P. J.; Ellis, D. J.; Heath, S. L. [Ru(η−cymene)Cl(pta)] (pta = 1,3,5-triaza-7-phosphatricyclo- [3.3.1.1]-decane): a water soluble compound that exhibits pH dependent DNA binding providing selectivity for diseased cells. *Chem. Commun.* **2001**, 1396−1397.

https://doi.org/10.1021/acs.inorgchem.2c03279
Inorg. Chem. 2022, 61, 20008−20025